Properties of a Simulated Convective Boundary Layer in an Idealized Supercell Thunderstorm Environment

CHRISTOPHER J. NOWOTARSKI,* PAUL M. MARKOWSKI, AND YVETTE P. RICHARDSON

Department of Meteorology, The Pennsylvania State University, University Park, Pennsylvania

GEORGE H. BRYAN

National Center for Atmospheric Research,+ Boulder, Colorado

(Manuscript received 1 November 2013, in final form 30 June 2014)

ABSTRACT

Nearly all previous numerical simulations of supercell thunderstorms have neglected surface fluxes of heat, moisture, and momentum. This choice precludes horizontal inhomogeneities associated with dry boundary layer convection in the near-storm environment. As part of a broader study on how mature supercell thunderstorms are affected by a convective boundary layer (CBL) with quasi-two-dimensional features (i.e., boundary layer rolls), this paper documents the methods used to develop a realistic CBL in an idealized environment supportive of supercells. The evolution and characteristics of the modeled CBL, including the horizontal variability of thermodynamic and kinematic quantities known to affect supercell evolution, are presented. The simulated rolls result in periodic bands of perturbations in temperature, moisture, convective available potential energy (CAPE), vertical wind shear, and storm-relative helicity (SRH). Vertical vorticity is shown to arise within the boundary layer through the tilting of ambient horizontal vorticity associated with the background shear by vertical velocity perturbations in the turbulent CBL. Sensitivity tests suggest that 200-m horizontal grid spacing is adequate to represent rolls using a large-eddy simulation (LES) approach.

1. Introduction

Over the past five decades, idealized numerical simulation studies of supercell thunderstorms have revealed a great deal about supercell dynamics and their sensitivity to the synoptic and mesoscale environment (Wilhelmson and Wicker 2001). Though they offer a degree of experimental control that is unmatched by observational studies, numerical simulations often neglect some physical processes that can affect supercell evolution. In particular, most previous studies have examined supercells in a steady, horizontally homogeneous environment and have neglected surface fluxes of heat, moisture, and momentum. In actual supercell environments, these surface fluxes act to produce a convective boundary layer (CBL) riddled with kinematic and thermodynamic inhomogeneities that evolve with time. The evolution of supercell thunderstorms is well known to be sensitive to average boundary layer properties. For instance, supercells are more likely to produce tornadoes in environments with increased low-level wind shear and moisture (e.g., Rasmussen and Blanchard 1998; Thompson et al. 2003; Markowski et al. 2003; Craven and Brooks 2004). Given such sensitivity, it would seem possible that the horizontal variations (on the meso-γ scale) in the properties of the low-level, near-storm environment caused by a CBL could also influence supercell evolution.

Previous studies have found sensitivity of deep moist convection to horizontal variations in the storm environment on the meso-β scale ($\sim$100 km; e.g., Atkins et al. 1999; Richardson 1999; Rasmussen et al. 2000; Richardson et al. 2007); however, investigations of the effects of meso-γ-scale ($\sim$10 km) heterogeneity on deep moist convection have been limited to very few studies, such as a numerical

* Current affiliation: Department of Atmospheric Sciences, Texas A&M University, College Station, Texas.

+ The National Center for Atmospheric Research is sponsored by the National Science Foundation.

Corresponding author address: Christopher J. Nowotarski, Department of Atmospheric Sciences, Texas A&M University, 3150 TAMU, College Station, TX 77843-3150.
E-mail: cjnowotarski@tamu.edu

DOI: 10.1175/MWR-D-13-00349.1

study of a cumulus congestus cloud in a CBL with no ambient shear (Carpenter et al. 1998) and a numerical study of a supercell in a poorly resolved CBL (Crook and Weisman 1998). Crook and Weisman discovered more rapidly developing gust front misovortices in simulations of supercells with a disorganized CBL. Furthermore, they found that the midlevel mesocyclone was more organized and the low-level gust front occlusion process was more fully developed in a horizontally homogeneous simulation than in those with a CBL. They speculated that CBL features may have disrupted storm organization, perhaps providing an explanation for the apparent increased likelihood of tornadogenesis in the evening as the boundary layer becomes less turbulent. Their study was limited by a relatively coarse horizontal grid spacing (750 m) and a relatively artificial mechanism for generating a CBL (a constant surface heat flux was applied). It remains unknown if these findings are robust, especially in a better-resolved boundary layer with convection organized in quasi-two-dimensional structures.

Given the low-level shear found in typical supercell thunderstorm environments, the CBL surrounding such storms is often organized in boundary layer rolls (hereafter rolls).[1] In general, CBL rolls are thermally direct, counterrotating horizontal vortices characterized by alternating bands (with a wavelength generally 2–3 times the CBL depth) of updrafts and downdrafts resulting from thermal and dynamic instabilities (e.g., Faller 1965; Lilly 1966; Brown 1972; Shirer 1986; Stensrud and Shirer 1988). Several theoretical studies (e.g., Asai 1970; Haack and Shirer 1992; Foster 2005) have identified the fastest-growing modes for various conditions as well as several possible orientations of the rolls relative to the shear vector or mean-flow vector. For CBLs in supercell environments, a combination of thermal and dynamic instabilities likely exists, such that the roll orientation is not easily generalized, though rolls are commonly found to be aligned nearly parallel to the mean vertical shear in the boundary layer (e.g., Kuo 1963; Asai 1970; Kuettner 1971; Shirer 1980; Etling and Brown 1993; Weckwerth et al. 1997).[2]

Observations suggest rolls are associated with considerable horizontal thermodynamic and kinematic variability in the CBL. Weckwerth et al. (1996) observed that potential temperature is 0.5 K higher and the water vapor mixing ratio is 1.5–2.5 $g\,kg^{-1}$ larger in the updraft branches of rolls than in areas of downdraft. Consequently, convective available potential energy (CAPE) is generally higher and lifting condensation levels are lower, likely providing thermodynamic advantage for deep moist convection there. Markowski and Richardson (2007) found that both the magnitude of the 0–1-km vector wind difference and 0–1-km storm-relative helicity (SRH) can vary significantly across the CBL. In one of their cases, the observed magnitude of horizontal variability in the 0–1-km vector wind difference (0–1 km SRH) associated with boundary layer convection was $>3\,m\,s^{-1}$ ($>50\,m^2\,s^{-2}$). Previously, horizontal variability associated with rolls has been studied as it relates to convection initiation (e.g., Wilson et al. 1992; Weckwerth et al. 1996; Xue and Martin 2006a,b) or misocyclone activity (e.g., Arnott et al. 2006; Marquis et al. 2007; Buban et al. 2012) along mesoscale boundaries such as the dryline or sea-breeze fronts; however, the effects of this variability on mature supercell thunderstorms remain largely unexplored.

The overarching goal of this study is to examine the effects of horizontal variability in the CBL on mature supercell thunderstorms as well as the influence an established supercell has on its surrounding environment. Here, we perform numerical simulations of an idealized supercell environment wherein a CBL is generated by the inclusion of radiation and land surface processes. In other work (Nowotarski 2013), supercells are simulated in this environment, and the effects of the CBL on supercells are isolated through comparison of the CBL simulation with a traditional horizontally homogeneous control simulation with similar average environmental properties. By varying the orientation of low-level shear vector relative to storm motion, we also study how supercells react to rolls with axes that are perpendicular or parallel to their motion.

Previous simulations of rolls employing mesoscale domains (e.g., Dailey and Fovell 1999; Peckham et al. 2004; Xue and Martin 2006a,b) have used a base-state environment more conducive to ordinary convection rather than the moderate- or high-shear environments conducive to supercell thunderstorms. These efforts have generally employed large-eddy simulation (LES) techniques with horizontal grid spacings ($\Delta_h > 500$ m) that may not adequately resolve rolls or their effects on deep convection. Higher-resolution LES of CBLs (e.g., Deardorff 1980; Moeng and Sullivan 1994; Weckwerth et al. 1997; Conzemius and Fedorovich 2008), while perhaps adequately representing rolls, have been limited by their small domain sizes or simple means of generating boundary layer instability (e.g., a constant surface heat flux). This study is unique in that it allows for the development of rolls in a model framework that includes

[1] For a more detailed discussion of boundary layer rolls (the body of work on this subject is prolific), the reader is referred to a number of extensive reviews on the subject (e.g., Brown 1980; Etling and Brown 1993; Atkinson and Zhang 1996; Young et al. 2002).

[2] Such rolls, under conditions with thermally unstable stratification, are often referred to as "horizontal convective rolls."

parameterizations of radiation and surface fluxes that may be subsequently affected by deep convection (e.g., cloud shading) in a domain large enough to accommodate a mature supercell thunderstorm.

Before initiating deep convection in the model, we first seek to understand the evolution and characteristics of the CBL in our idealized supercell environment and verify that our model is configured appropriately to represent both rolls and deep moist convection. This article focuses on the development of the CBL that serves as the base state for subsequent supercell simulations (Nowotarski 2013). The next section documents the numerical modeling methods. Section 3 presents results of the CBL simulations concerning the characteristics of the rolls, including horizontal variability in parameters likely to affect subsequent supercell evolution, and the development of vertical vorticity within the boundary layer is discussed in section 4. Section 5 presents sensitivity tests to horizontal grid resolution, verifying the suitability of the model configuration. Some final summary remarks and a discussion of the implications of the results for supercell thunderstorms are offered in the last section.

2. Methods

Our goal of simulating a supercell thunderstorm within a CBL composed of rolls is challenging because simulation of a CBL requires small grid spacing of $O(100)$ m and simulation of an entire supercell thunderstorm requires a large domain of $O(100)$ km. To approach this problem, we first simulate a CBL alone (i.e., without a supercell) with the intention of later initializing deep convection. Herein we describe an effective way to simulate realistic rolls. Our simulations start from a laminar, statically stable boundary layer. The boundary layer is gradually destabilized through surface heating forced by a radiative flux, and within a few hours there is a transition to a turbulent CBL that deepens with time. Through trial and error, we determined the following model configuration, base state, and initialization method for developing and sustaining rolls for at least a 2-h period (the required time for subsequent supercell simulations).

a. Numerical model configuration

The idealized CBL simulations in this study and subsequent supercell simulations were performed using the cloud model, release 15 (CM1; Bryan and Fritsch 2002; Bryan 2002). CM1 is a nonhydrostatic model that includes moisture and is well suited for the idealized simulation of mesoscale atmospheric phenomena. The compressible governing equations are solved on an Arakawa C grid (Arakawa and Lamb 1977) with split time steps for more frequent (6 times as often) solving of acoustic wave terms (Klemp and Wilhelmson 1978). The model uses third-order Runge–Kutta time differencing for integration and fifth-order spatial derivatives for advection (Wicker and Skamarock 2002). Subgrid-scale (SGS) turbulence is parameterized using a 1.5-order turbulence kinetic energy (TKE) closure scheme similar to that of Deardorff (1980), but with a larger constant in the dissipation rate (following Moeng and Wyngaard 1988) and no increase in this constant near the lower surface. In all simulations, the Coriolis force is neglected because it was not found to be necessary to organize boundary layer convection into rolls. Radiation is parameterized using a vertical column model with the National Aeronautics and Space Administration (NASA)–Goddard formulations for both long and shortwave interactions with air and water species (Tao et al. 1996; Chou et al. 1998; Chou and Suarez 1999; Chou et al. 1999). Precipitation microphysics, parameterized with the NASA–Goddard Cumulus Ensemble formulation (Tao and Simpson 1993) of the Lin et al. (1983) scheme (hereafter the LFO scheme), is included primarily to facilitate later supercell simulations. Though shallow, transient clouds do form atop the CBL in our simulations, their effects on the radiation budget are negligible.

For the CBL simulations, surface fluxes of heat, moisture, and momentum are modeled using a Monin–Obukhov similarity theory surface-layer model. Surface soil conditions are modeled using a five-layer thermal diffusion scheme. Soil moisture availability is held fixed. For details on these parameterizations, the reader is referred to Grell et al. (1994). These schemes require a user-specified land-use type. For this study, a land-use type corresponding to ''irrigated cropland'' was selected.[3] This land-use type was chosen because its relatively high moisture availability (50%) was found to promote longer-lasting roll structures in the boundary layer. We note that surface buoyancy flux decreases as surface moisture availability increases, owing to a lower Bowen ratio; thus, the influence of buoyancy relative to shear in organizing boundary layer convection is slowed relative to that with a drier surface, allowing rolls to persist longer (see section 5).

A horizontal domain size of 250 km × 200 km is chosen for the full-domain, ''supercell-ready,'' CBL

[3] Necessary parameters for the land surface model are defined in a U.S. Geological Survey reference table. For irrigated cropland they are as follows: albedo = 0.18, moisture availability = 0.5, surface emissivity = 0.985, roughness length = 0.1 m, and thermal inertia = 0.04 J m^{-2} K^{-1} s$^{-0.5}$.

TABLE 1. Summary of domain and time step configurations for full-domain and sensitivity test CBL simulations.

	Horizontal grid spacing		
	100 m	200 m	500 m
Full domain N_x, N_y	—	1248, 992	—
CBL test N_x, N_y	400, 400	200, 200	80, 80
N_z	99	99	99
Min Δz, Max Δz	50, 500 m	50, 500 m	50, 500 m
Large Δt	0.75 s	0.75 s	2 s
Acoustic Δt	0.125 s	0.125 s	0.333 s

simulations presented here. Because coupled atmospheric radiation and land surface models are used to initiate boundary layer convection, grid translation for supercell simulations is not practical. Thus, the domain for the CBL simulations described herein must be large enough to eventually accommodate a supercell thunderstorm for a 2-h simulation duration while preventing the dynamically interesting portions of the storm from approaching the lateral boundaries. Horizontal grid spacing is constant across the domain and identical in the x and y directions. The sensitivity of the CBL to horizontal grid spacing was tested on a smaller domain (40 km × 40 km) with three horizontal grid spacings: 100, 200, and 500 m (results of this test are presented in section 5). As will be discussed, horizontal grid spacing of 200 m was found to adequately resolve rolls; therefore, this grid spacing was chosen for the large-domain CBL simulations. The number of grid points in each direction and the necessary model integration time steps to maintain computational stability are shown for each horizontal grid spacing in Table 1. In all simulations, the domain is 18 km deep and the vertical grid is stretched from 50-m spacing in the lowest 3 km to 500 m above 8.5 km to provide increased resolution of the boundary layer. The upper and lower boundaries are rigid walls, and a Rayleigh sponge layer is applied above 14 km to damp vertically propagating gravity waves. Surface drag is parameterized using Monin–Obukhov similarity theory [see Grell et al. (1994) for further details] with a roughness length z_0 determined by the land-use type ($z_0 = 0.1$ m for irrigated cropland). All lateral boundary conditions are periodic. For more detailed information regarding the model configuration, the reader is referred to Nowotarski (2013).

b. Base state and initialization

The CBL simulations are initialized with horizontally homogeneous base states supportive of both rolls and supercell thunderstorms. Base-state quantities are denoted by overbars, and they are defined as horizontal averages of the environment, which are dependent on both height and time because of the inclusion of surface fluxes. Initial-state or initial-base-state quantities are base-state quantities at $t = 0$, and they are denoted with a subscript 0. The initial thermodynamic profiles (Fig. 1) are modified versions of the Weisman and Klemp (1982) analytic profiles of initial base-state potential temperature θ_0 and water vapor mixing ratio q_{v_0} defined by

$$\theta_0(z) = \begin{cases} \theta_{\text{sfc}} + z\left(\dfrac{d\theta_0}{dz}\right)_1, & z \le z_1 \\ \theta_{z_1} + (z - z_1)\left(\dfrac{d\theta_0}{dz}\right)_2, & z_1 < z \le z_2 \\ \theta_{z_2} + (\theta_{\text{tr}} - \theta_{z_2})\left(\dfrac{z}{z_{\text{tr}}}\right)^{5/4}, & z_2 < z \le z_{\text{tr}} \\ \theta_{\text{tr}} \exp\left[\dfrac{g}{c_p T_{\text{tr}}}(z - z_{\text{tr}})\right], & z > z_{\text{tr}} \end{cases}, \quad (1)$$

and

$$q_{v_0}(z) = \begin{cases} q_{v_{\text{sfc}}} - z\left[\dfrac{(q_{v_{\text{sfc}}} - q_{v_1})}{z_1}\right], & z \le z_1 \\ q_{v_1} - (z - z_1)\left[\dfrac{(q_{v_1} - q_{v_2})}{z_2 - z_1}\right], & z_1 < z \le z_2 \\ q_{v_2} + (z - z_2)\left(\dfrac{dq_{v_0}}{dz}\right), & z_2 < z \le z_{\text{tr}} \\ q_{v_{\text{tr}}}, & z > z_{\text{tr}} \end{cases}, \quad (2)$$

where g is the acceleration due to gravity and c_p is the specific heat capacity of dry air. The tropopause height z_{tr} is 12 km, the tropopause potential temperature $\theta_{\text{tr}} = 343$ K, the tropopause temperature $T_{\text{tr}} = 213$ K, and the tropopause mixing ratio $q_{v_{\text{tr}}} = 0.06\ \text{g kg}^{-1}$. Two potential temperature inversions are added to the lower levels of the profile to ensure slow development and adequate capping of future convection. The first represents a statically stable nocturnal boundary layer commonly found in morning soundings and extends from the surface, where $\theta_{\text{sfc}} = 295$ K, to a height $z_1 = 1000$ m with a vertical potential temperature gradient $(d\theta_0/dz)_1 = 0.009\ \text{K m}^{-1}$. The second extends from 1000 m to a height $z_2 = 1500$ m with $(d\theta_0/dz)_2 = 0.002\ \text{K m}^{-1}$. Water vapor mixing ratio is set at the surface, $q_{v_{\text{sfc}}} = 14\ \text{g kg}^{-1}$; the top of the first inversion,

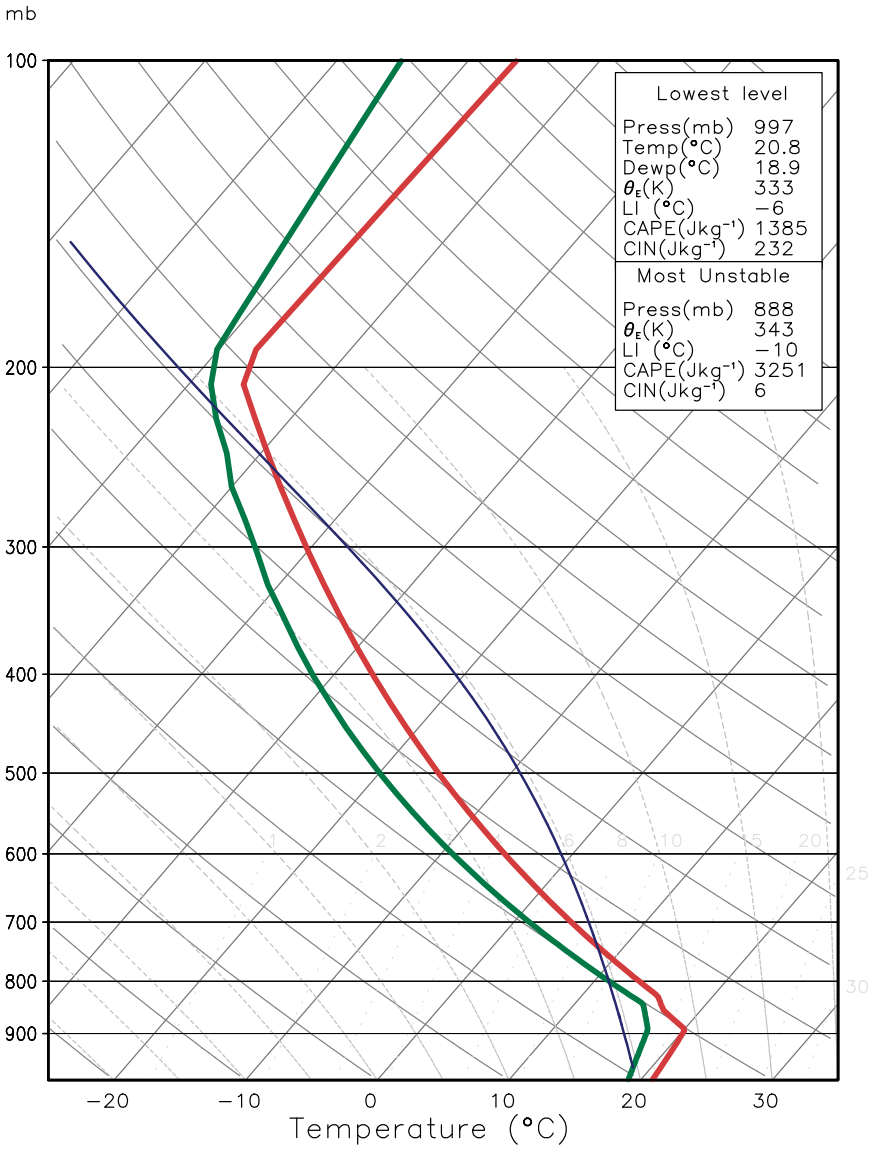

FIG. 1. Skew T–log$p$ diagram showing the initial base-state temperature (red) and dewpoint temperature (green) profiles used to initialize CBL simulations. The blue line shows the temperature of a lifted surface parcel.

$q_{v_1} = 14\,\mathrm{g\,kg^{-1}}$; and the top of the second inversion, $q_{v_2} = 13\,\mathrm{g\,kg^{-1}}$. The vertical gradient of moisture in the troposphere above z_2 is $dq_{v_0}/dz = -1.2\,\mathrm{g\,kg^{-1}}$. The initial state is in hydrostatic balance with a surface pressure of 1000 hPa. The resulting environment has surface-based CAPE [convective inhibition (CIN)] of 1385 [232] J kg^{-1}.

Two base-state wind profiles are used for the CBL simulations, each resulting in a different orientation of boundary layer convection relative to subsequent right-moving supercell motion. Both are variants of the clockwise, quarter-turn hodograph used by Weisman and Klemp (1986) with initial vertical profiles of horizontal components of momentum defined by

$$u_0(z) = \begin{cases} u_1 - u_1 \cos\left(\dfrac{\pi}{2}\dfrac{z}{z_1}\right) + u_{\mathrm{sfc}}, & z \le z_1 \\ u_1 + (z - z_1)\left(\dfrac{u_2 - u_1}{z_2 - z_1}\right) + u_{\mathrm{sfc}}, & z_1 < z \le z_2 \\ u_2 + u_{\mathrm{sfc}}, & z > z_2 \end{cases}, \tag{3}$$

and

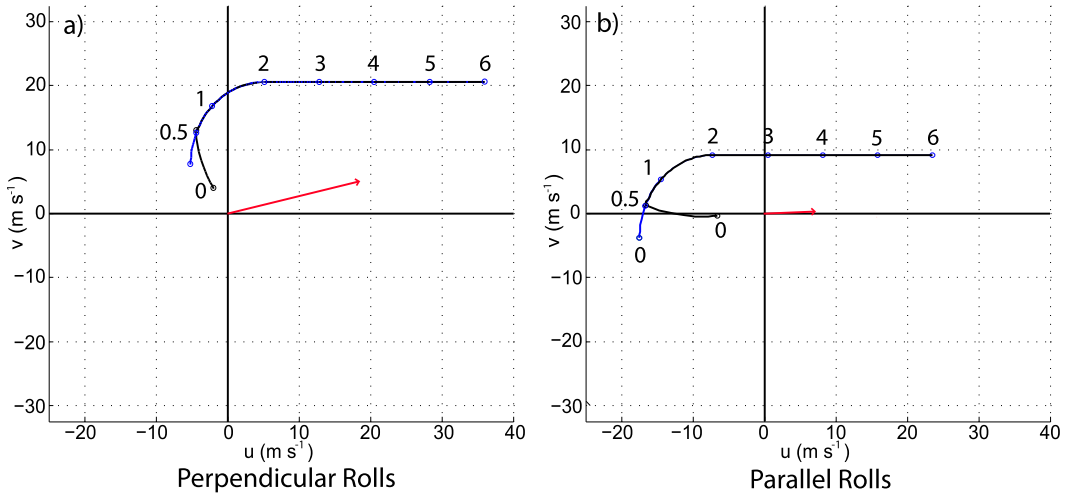

FIG. 2. Base-state hodographs used to initialize CBL simulations (blue) and the domain-averaged hodographs when rolls first form at $t = 180$ min (black) in the simulations with rolls (a) perpendicular to and (b) parallel to the predicted right-moving mature supercell motion (red arrows). Heights above the ground on each hodograph are labeled in km.

$$v_0(z) = \begin{cases} v_1 \sin\left(\dfrac{\pi}{2}\dfrac{z}{z_1}\right) + v_{\text{sfc}}, & z \le z_1 \\ v_1 + v_{\text{sfc}}, & z > z_1 \end{cases}, \qquad (4)$$

where z_1 is the height over which the wind profile is curved and z_2 is the height above which the wind is constant. In both cases $z_1 = 2$ km and $z_2 = 6$ km. For the case of rolls perpendicular to the right-moving supercell storm motion (hereafter perpendicular rolls), the initial profile (Fig. 2a, blue) has $u_{\text{sfc}}, v_{\text{sfc}} = -5, 8\,\text{m s}^{-1}$; $u_1, v_1 = 10.25, 13\,\text{m s}^{-1}$; and $u_2, v_2 = 41, 13\,\text{m s}^{-1}$. The initial 0–3-km SRH for the perpendicular-roll environment is $506\,\text{m}^2\,\text{s}^{-2}$. Simulations with rolls parallel to storm motion (hereafter parallel rolls) have an initial wind profile (Fig. 2b, blue) with $u_{\text{sfc}}, v_{\text{sfc}} = -17, -4\,\text{m s}^{-1}$; $u_1, v_1 = -7, 9.5\,\text{m s}^{-1}$; and $u_2, v_2 = 23, 9.5\,\text{m s}^{-1}$. The SRH for the parallel roll environment is $379\,\text{m}^2\,\text{s}^{-2}$.

Because there is no large-scale horizontal pressure gradient in the simulation (and additional terms needed to balance it, e.g., Coriolis acceleration), there is no mechanism to counteract surface drag and turbulent mixing, which act to decrease low-level vertical wind shear in the CBL over time. Consequently, as discussed below, simulated rolls may transition to disorganized convection more rapidly than in nature. Despite this drawback, we chose to

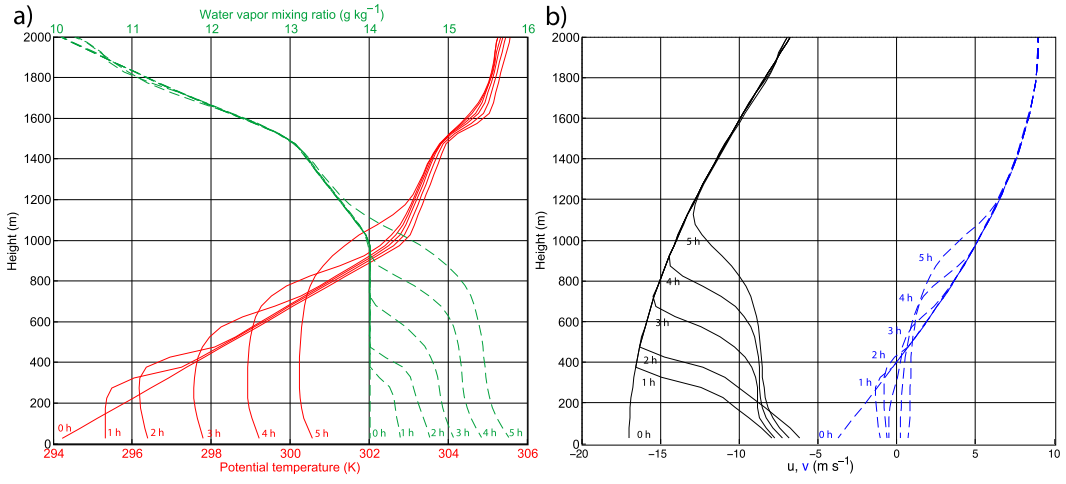

FIG. 3. Time evolution of (a) domain-averaged potential temperature (red) and water vapor mixing ratio (dashed green) profiles and (b) domain-averaged u (black) and v (dashed blue) wind component profiles in the parallel-roll CBL simulation with 200-m horizontal grid spacing. Note that owing to roll orientation, u is largely the along-roll component of the wind, and v is largely the cross-roll component.

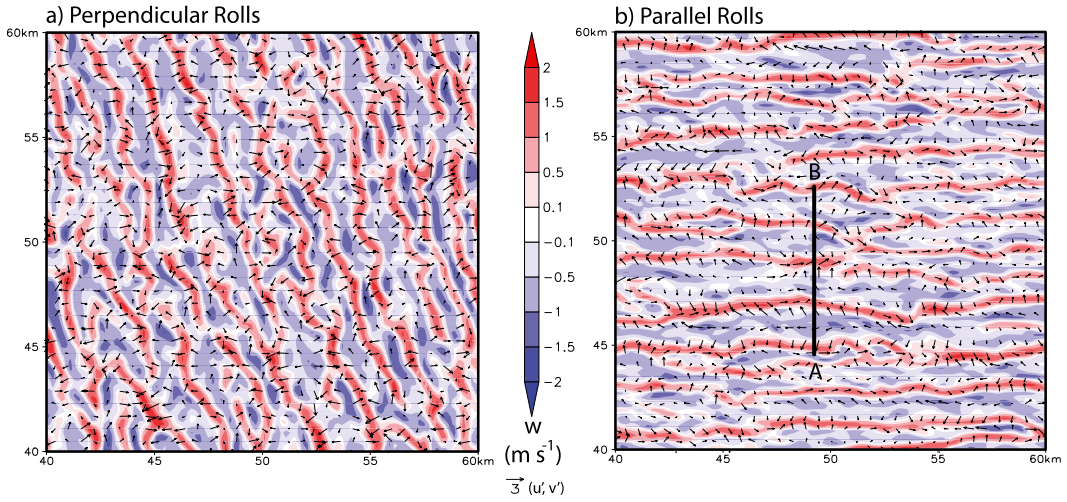

FIG. 4. Horizontal cross sections of vertical velocity at 225 m above the lower model surface in 200-m horizontal grid spacing CBL simulations at $t = 3.75$ h for rolls (a) perpendicular and (b) parallel to predicted right-moving supercell motion. The black line in (b) shows the location of the vertical cross section for Fig. 5. Vectors indicate perturbation winds at $z = 25$ m.

neglect a large-scale pressure gradient in order to simplify the experiment design and the analysis of subsequent simulated supercells. For the relatively strong initial vertical shear associated with supercells, and the relatively weak surface buoyancy flux in this case, we found the initial low-level shear can persist for the period required to examine roll effects on supercells (2 h).

Both perpendicular and parallel rolls in the CBL simulations are initialized by inserting random potential temperature perturbations with maximum amplitude of ±0.1 K in the lowest 1 km of the model domain. The initial deep and surface soil temperatures are set to 295 K, the temperature at the lowest scalar grid level in the model. The initial radiation tendencies are representative of a location in north-central Oklahoma at 1200 UTC 15 May. As the model is advanced, radiation tendencies are updated every 300 s, such that the soil is heated by increasing amounts of shortwave radiation corresponding to the morning increase in insolation. The resulting increase in the surface sensible heat flux causes a superadiabatic surface layer to develop. This instability is eventually released in the form of boundary layer convection, which soon organizes into rolls. The CBL simulations are run for 28 800 s (8 h), simulating the entire morning and early afternoon evolution of a CBL.

3. CBL characteristics

a. General evolution

In general, the simulated CBL development is consistent with observations (e.g., Kuettner 1959; LeMone 1973; Weckwerth et al. 1999) and previous simulation studies (e.g., Dailey and Fovell 1999; Peckham et al. 2004; Xue and Martin 2006a,b). As incoming shortwave radiation increases in the simulation, surface heat and moisture fluxes act to destabilize and moisten the boundary layer (Fig. 3a). For the first few hours the resolved-scale flow is weakly turbulent (see section 5), and the mixed layer deepens with time almost entirely through parameterized SGS turbulence.

Three hours (10 800 s) after model initiation, dry (i.e., subsaturated) boundary layer convection with vertical velocity magnitudes exceeding $1\ \mathrm{m\ s^{-1}}$ commences across the entire domain. The timing of the initiation of this convection is largely dependent on the horizontal grid spacing (see section 5). Immediately, the convection organizes into long, relatively small wavelength (where wavelength refers to the spacing between roll updrafts) rolls with strong linearity.[4] By roll initiation time, surface drag and SGS mixing have modified the low-level winds (Fig. 2, black hodographs; Fig. 3b). In both the perpendicular (Fig. 4a) and parallel (Fig. 4b) cases, the axes of the rolls are aligned with both the mean boundary layer wind and boundary layer shear vector (cf. 0–500-m layer of hodographs in Fig. 2).

Over the lifetime of the rolls, their wavelength increases from 1500 to 2250 m while their aspect ratio (i.e., the ratio of wavelength to boundary layer depth) remains nearly constant between 2.5 and 3.0 because of the concurrently deepening boundary layer. Roll linearity

[4] Linearity refers to the amount of along-roll variation, such that strong (weak) linearity corresponds to little (significant) along-roll variation.

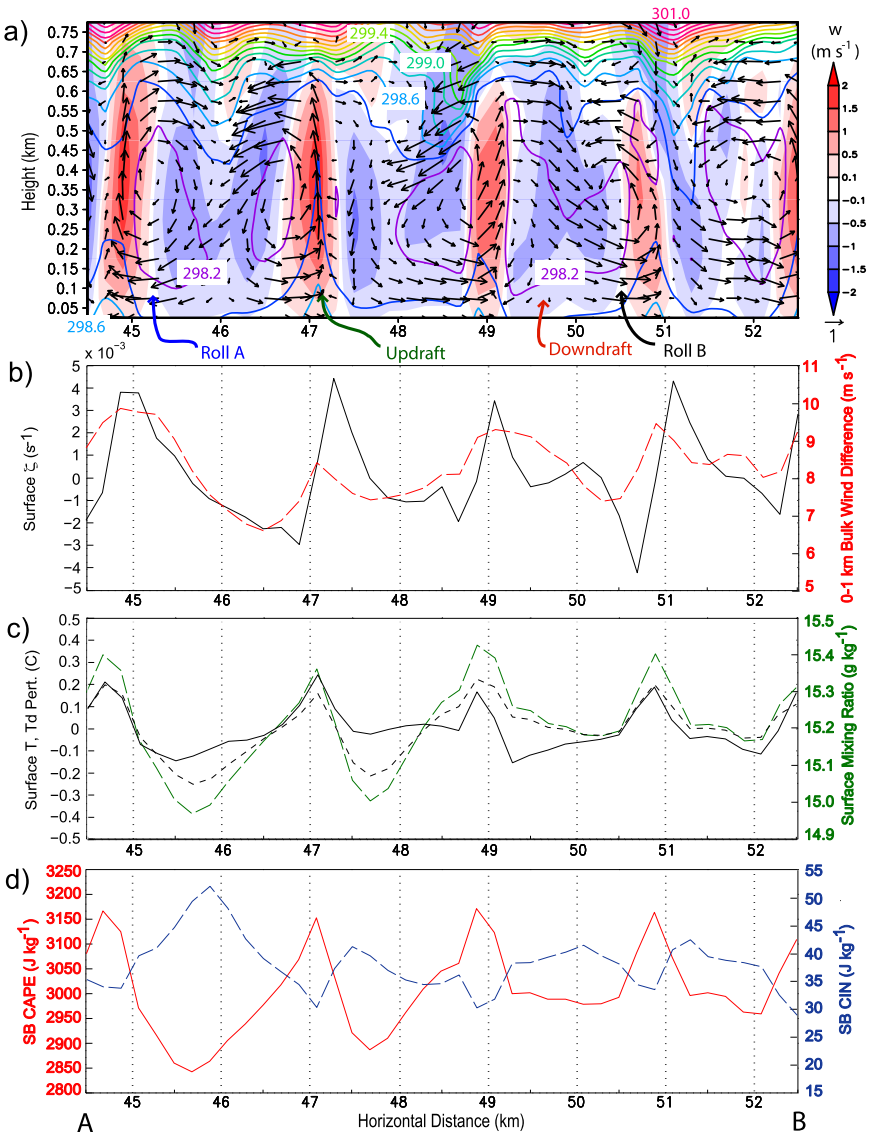

FIG. 5. (a) Vertical cross section of the parallel-roll CBL simulation along the black line in Fig. 4b at $t = 3.75$ h. Vertical velocity ($m\,s^{-1}$) is shaded, potential temperature is contoured at 0.2-K intervals (from 298.2 to 301.0 K), and perturbation velocity ($m\,s^{-1}$) in the plane of the cross section is shown with arrows. (b) Values of vertical vorticity ($\times 10^{-3}\,s^{-1}$, black) at the lowest model level and 0–1-km bulk wind difference ($m\,s^{-1}$, red dashed) along the same cross section. (c) Temperature perturbation (°C, black solid), dewpoint temperature perturbation (°C, black short dashed), and water vapor mixing ratio ($g\,kg^{-1}$, green long dashed) from the lowest grid level. (d) Surface-based CAPE ($J\,kg^{-1}$, red) and surface-based CIN ($J\,kg^{-1}$, blue dashed).

decreases with time, and the boundary layer transitions to disorganized convection approximately 2 h after roll formation.

b. Thermodynamic variability

The CBL simulations at 3.75 h (1 h after roll formation and the midpoint of subsequent supercell simulations) show considerable horizontal variability in the thermodynamic fields within the boundary layer [hereafter, unless otherwise stated, "variability" refers to horizontal variations on the scale of the wavelength of rolls (<5 km)]. Figure 5 shows a vertical cross section of the boundary layer in the simulation with rolls parallel to potential right-moving supercell motion (see Fig. 4b for cross-sectional location) with various thermodynamic and kinematic properties plotted along the cross section. Potential temperature (Figs. 5a,c) near the surface is as much as 0.3 K higher (lower) than the

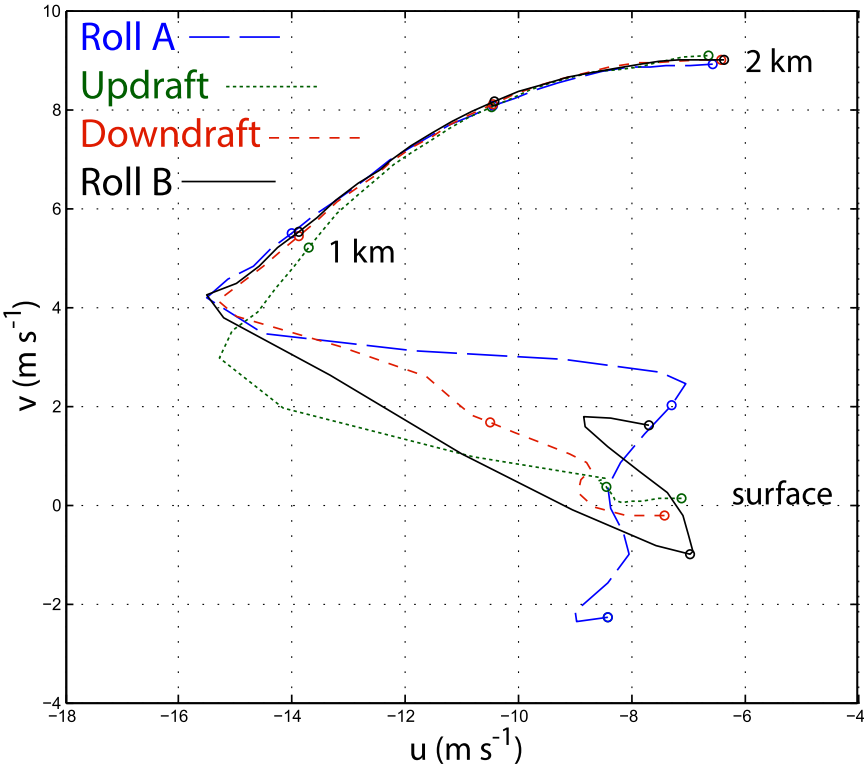

FIG. 6. Hodographs at four points indicated in Fig. 5a from $z = 0$ to 2 km in the parallel BASE simulation at $t = 3.75$ h. Circles indicate heights above the lower model surface at 500-m intervals.

horizontal average in regions of updraft (downdraft). This surface variability is consistent with the observations of Weckwerth et al. (1996), who found horizontal potential temperature differences of approximately 0.5 K between updraft and downdraft. At the top of the boundary layer, downdraft regions tend to be in phase with higher potential temperatures. For instance, $z = 600$ m is the approximate depth of the boundary layer z_i at this time, where z_i is defined as the height where the domain-averaged heat flux $\overline{w'\theta'}$ is a minimum [following the method of Deardorff (1974)]. At this height, downdraft regions are as much as 1 K warmer than updraft regions, because the capping inversion extends below z_i (an average quantity) in downdrafts and the mixed layer penetrates above z_i in updrafts. This is consistent with a range of observations of potential temperature variability toward the top of the boundary layer (0.1–3.0 K; LeMone and Pennell 1976; Atlas et al. 1986).

The simulated rolls also lead to horizontal variability of moisture in the CBL. Water vapor mixing ratio, q_v, generally varies less than 0.5 g kg^{-1} at the lowest grid level across the rolls (Fig. 5c), but farther aloft in the CBL q_v may differ by as much as 1 g kg^{-1} (not shown). Like potential temperature, this variability is also within the range found in observational studies (~0.1–3.5 g kg^{-1}; e.g., LeMone and Pennell 1976; Reinking et al. 1981; Weckwerth et al. 1996).

As a result of boundary layer variability in temperature and moisture, thermodynamic parameters relevant to deep convection such as dewpoint temperature, CAPE, and CIN also vary across rolls. Dewpoint temperature is about 0.5 K higher near the surface in warm, moist updraft regions of rolls than in the cooler, dry downdrafts (Fig. 5c). Surface-based CAPE (SBCAPE) varies by as much as 300 J kg^{-1} (~10%) across rolls, with higher values in updrafts, whereas the magnitude of surface-based CIN (SBCIN) can be reduced by up to 22 J kg^{-1} (~40%) in updrafts. Similar variability exists in mixed-layer[5] CAPE and CIN. All this suggests conditions for deep convection are more favorable in roll updrafts. This variability is notably less than that observed by Weckwerth et al. (1996); they measured dewpoint temperature variations of 2–3 K, which are much larger than those simulated here. This discrepancy is likely due to the relatively steep decline in moisture above the boundary layer in their study when compared with these simulations where $q_{v_0} = 14$ g kg^{-1} up

[5] In this case, the mixed layer was prescribed as the average depth of the CBL at $t = 3.75$ h.

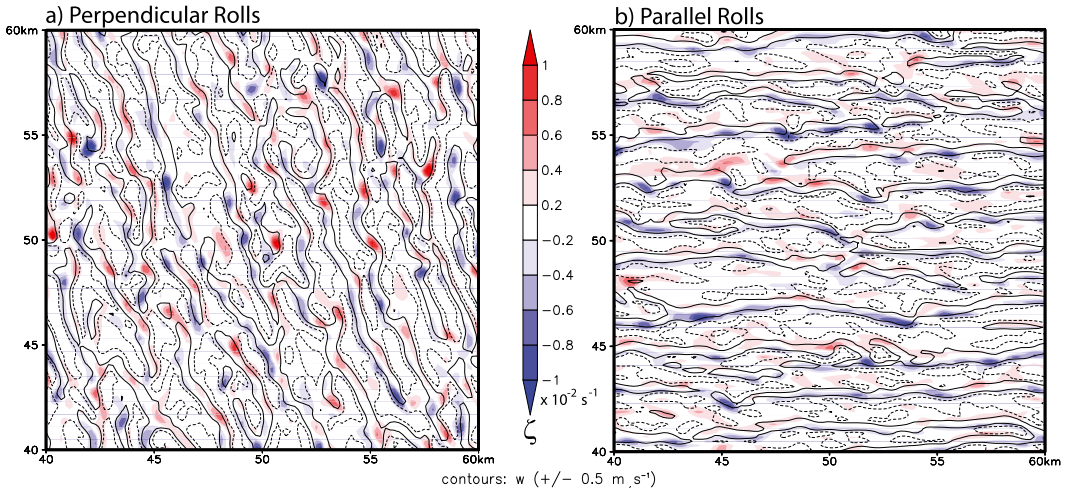

FIG. 7. As in Fig. 4, but with vertical vorticity at the lowest model level ($z = 25$ m) shaded. Solid (dashed) contours indicate locations where vertical velocity is greater (less) than $+(-)0.5\,\mathrm{m\,s^{-1}}$ at $z = 225$ m.

to 1 km (Figs. 1 and 3). Though surface moisture flux increases q_v in the boundary layer with time (especially in updraft branches), the layer of relatively moist air above the boundary layer (600–1000 m) limits the entrainment of dry air from the free troposphere into the boundary layer.

c. *Kinematic variability*

Rolls are easily identified in horizontal cross sections of vertical velocity, with alternating bands of updrafts and downdrafts characterizing the simulated CBL. Updraft regions are generally narrower than downdraft branches, and they have larger vertical velocity magnitude (Figs. 4 and 5a). This is consistent with positive resolved vertical velocity skewness in the boundary layer (not shown), which gradually increases as the rolls become disorganized with time. One hour after roll formation ($t = 3.75$ h) the maximum (minimum) vertical velocity in the CBL is $3.3\,(-2.3)\,\mathrm{m\,s^{-1}}$. The largest vertical velocity magnitudes are generally found in the central or upper portions of the CBL. An hour later ($t = 4.75$ h) as the CBL becomes more disorganized, the range of vertical velocity expands to between -3.5 and $4.5\,\mathrm{m\,s^{-1}}$. This increase in magnitude is a reflection of the increasing surface buoyancy flux over time. The magnitude of vertical velocity perturbations within the simulated CBL is generally less than $5\,\mathrm{m\,s^{-1}}$ at all times and all heights. Furthermore, there is little difference in vertical velocities between the parallel- and perpendicular-roll simulations.

Vertical motions within the CBL act to mix horizontal momentum, resulting in perturbations to the horizontal flow. Near the surface, perturbation winds are generally less than $5\,\mathrm{m\,s^{-1}}$ with convergent flow beneath updraft branches and divergence in regions of downdraft (Figs. 4 and 5a). Because there is little variation in wind direction (cf. Fig. 2; south-southeasterly in the perpendicular case and easterly in the parallel-roll case) over the depth of the boundary layer, but wind speed increases with height, there is a negative flux of along-roll momentum near the ground such that along-roll wind speed is greater in downdrafts than updrafts.

Figure 6 shows four low-level hodographs from selected locations along the cross section in Fig. 5 illustrating the variability in the parallel-roll simulation. Whereas updraft (green) and downdraft (red) winds are

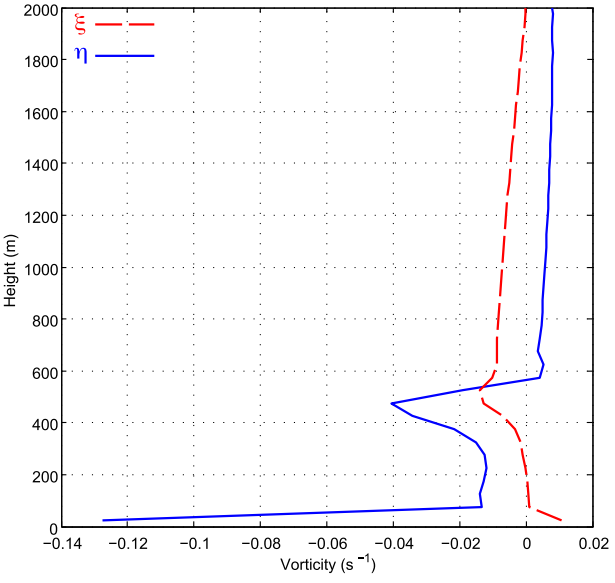

FIG. 8. Vertical profiles of horizontally averaged horizontal vorticity components at $t = 2.5$ h in the parallel-roll CBL simulation; ξ (red dashed) is the eastward component and η (blue) is the northward component.

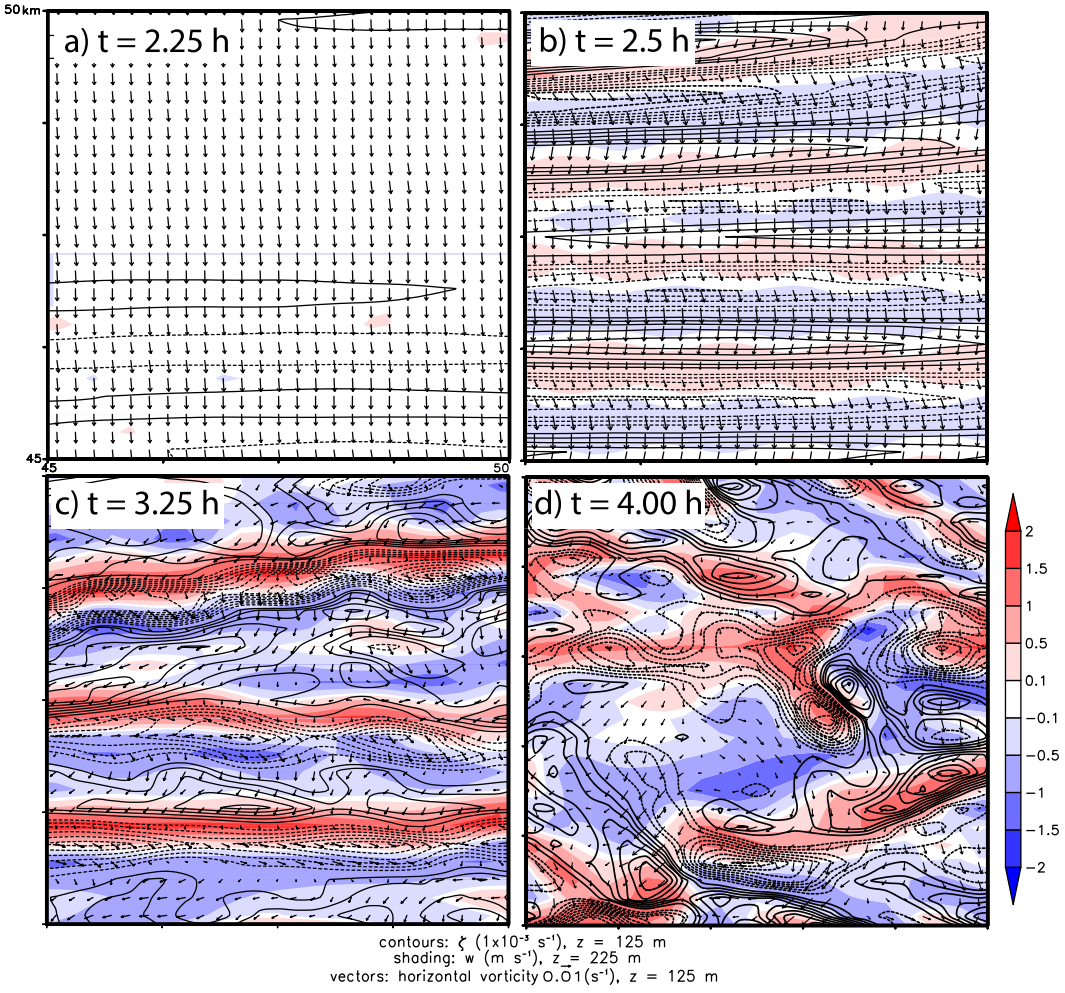

FIG. 9. Horizontal cross sections of the parallel-roll CBL simulation at (a) 2.25, (b) 2.5, (c) 3.25, and (d) 4.0 h. Vertical vorticity at $z = 125$ m is contoured in increments of $1 \times 10^{-3}\,\mathrm{s}^{-1}$. Vertical velocity at $z = 225$ m is shaded in $\mathrm{m\,s}^{-1}$ and horizontal vorticity at $z = 125$ m is shown with vectors scaled in s^{-1} according to the legend.

similarly oriented over the lowest 1 km in the along-roll direction (easterly), wind speed in the surface-to-500-m layer is reduced in the updraft region. Roll A (blue) and roll B (black), which are representative of rolls with opposite circulations, have similar along-roll velocities in the CBL but opposing low-level momentum and shear in the cross-roll direction (in this case, y). Despite lower overall values in the parallel-roll case than the perpendicular-roll case (not shown), Fig. 5b shows that 0–1-km vector wind difference can differ by as much as 5–6 $\mathrm{m\,s}^{-1}$ across rolls. SRH over the lowest 0–1 km is calculated using storm motions from the supercell simulations and varies by 60 (30) $\mathrm{m}^2\,\mathrm{s}^{-2}$ in the perpendicular- (parallel-) roll simulation. Boundary layer hodograph and shear variations of similar magnitudes were observed by Markowski and Richardson (2007, see their Fig. 10b).

4. Vertical vorticity in the CBL

Unlike traditional idealized simulations of deep convection that use horizontally homogeneous environments (i.e., there are no horizontal variations of any length scale in the environment), our simulated CBL environments with rolls locally contain nonzero vertical vorticity. Initially, bands of both positive (cyclonic) and negative (anticyclonic) vertical vorticity, ζ, of magnitudes reaching the order of $10^{-3}\,\mathrm{s}^{-1}$ develop in regions of strong horizontal gradients of vertical velocity between updraft and downdraft branches. Marquis et al. (2007) observed similar alternating bands of vertical vorticity in the CBL that were associated with linear horizontal structures well away from their interactions with a mesoscale boundary. As the rolls intensify and linearity decreases, bands of ζ become more three-dimensional as they break into

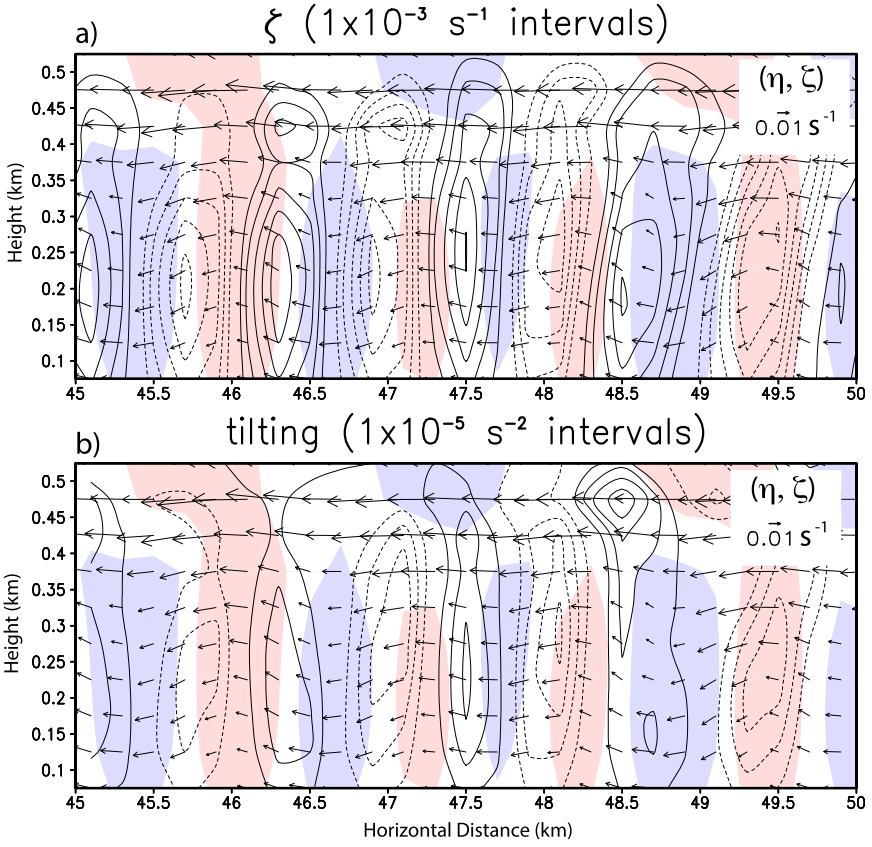

FIG. 10. Vertical cross sections in the y–z plane of the parallel-roll CBL simulation at 2.5 h of (a) vertical vorticity and (b) the tilting term in the vertical vorticity tendency equation. In both plots, vectors are vorticity within the plane of the cross section, and vertical velocity greater (less) than $+(-)0.1\,\mathrm{m\,s^{-1}}$ is shaded in red (blue).

individual vorticity extrema (Fig. 7), with ζ magnitudes as high as $2 \times 10^{-2}\,\mathrm{s^{-1}}$ and a horizontal diameter of ~1 km. These areas of ζ are of similar magnitude over the entire depth of the CBL, including the near-surface region. Past studies (Markowski and Hannon 2006; Arnott et al. 2006) have observed similar vorticity extrema in a CBL using mobile Doppler radar, and Kanak et al. (2000) simulated similar CBL vortices with a numerical model.

Several studies have examined vertical vorticity in the context of boundary layer rolls, but most have focused on roll interactions with a mesoscale boundary in the context of convection initiation. For instance, Atkins et al. (1995) showed with observations how rolls may be lifted over a sea-breeze front such that their inherent horizontal vorticity is tilted into the vertical. Dailey and Fovell (1999) verified this finding with numerical simulations. In these cases, the development of significant vertical vorticity was explained through tilting of roll vorticity by horizontal gradients in vertical velocity associated with the sea-breeze front. Other studies (e.g., Wilson et al. 1992; Xue and Martin 2006b; Marquis et al. 2007) have shown how rolls may modulate the formation of misocyclones by concentrating background vertical vorticity associated with horizontal shear zones along boundaries. Unfortunately, those studies cannot explain the mechanism by which vertical vorticity is generated in the CBL in the simulations of this study, where there is no mesoscale boundary present.

Our simulations (Fig. 7) and previous studies show that vertical vortices exist in the CBL *without* the aid of mesoscale boundaries. Markowski and Hannon (2006) observed patches of vertical vorticity both along and away from an outflow boundary. They found that stretching of vertical vorticity was important in amplifying vorticity extrema, but they could not conclusively identify the initial source of vertical vorticity in the boundary layer. Marquis et al. (2007) suggested that the linear patterns of vertical vorticity observed in the boundary layer were consistent with the tilting of environmental horizontal vorticity by alternating updraft and downdraft bands in the CBL, but they were unable to verify this hypothesis by isolating the CBL from the

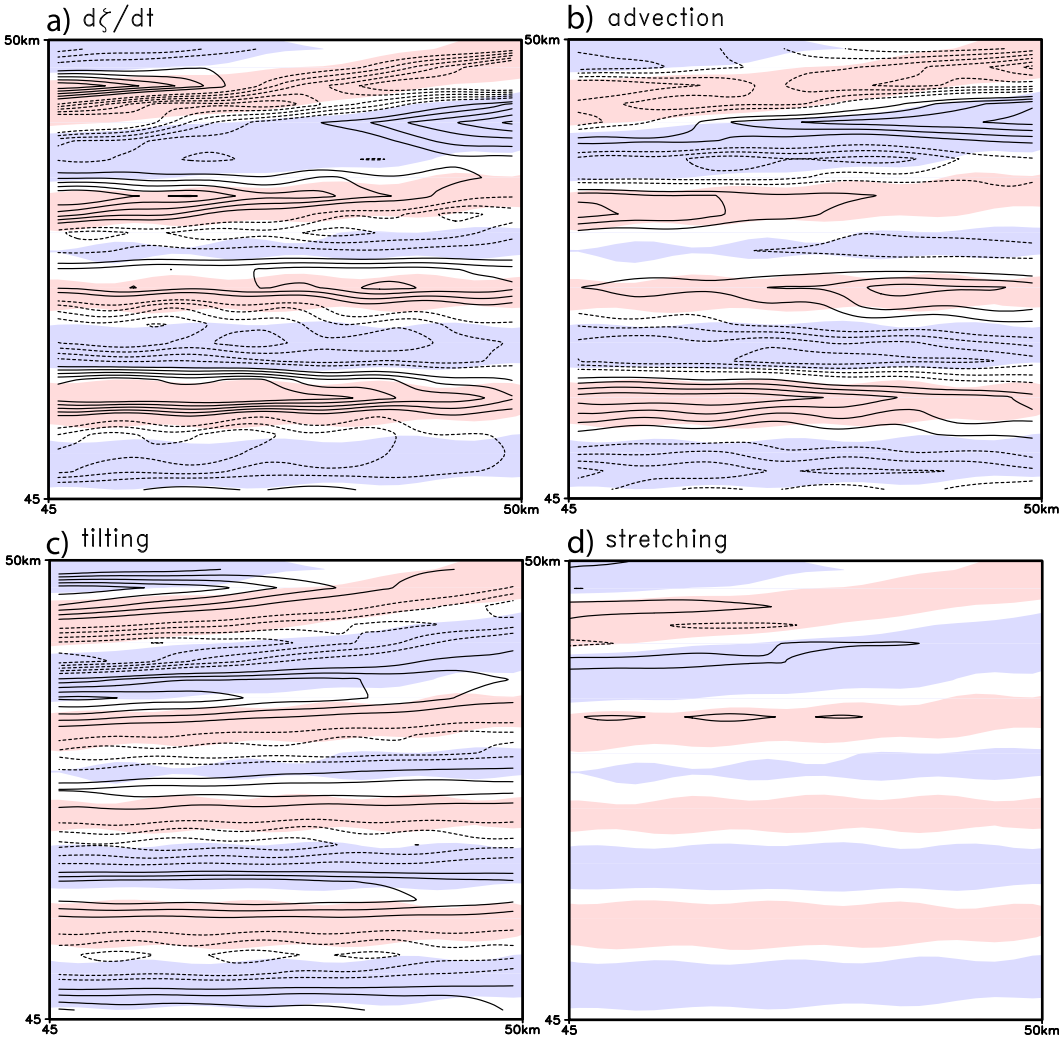

FIG. 11. Horizontal cross sections of (a) local vertical vorticity tendency, (b) advection, (c) tilting, and (d) stretching at 2.5 h at $z = 75$ m. Areas with vertical velocity greater (less) than $+(-)0.1\,\mathrm{m\,s^{-1}}$ are shaded in red (blue) All contours are at $5 \times 10^{-6}\,\mathrm{s^{-2}}$ intervals.

effects of the nearby mesoscale boundaries. Maxworthy (1973) suggested a mechanism by which existing vortices might tilt horizontal vorticity in the surface layer as a means of amplifying and maintaining their vertical vorticity. Their study was also unable to determine a mechanism for the initial generation of vertical vorticity. In simulations with no mean flow or vertical shear, Kanak et al. (2000) suggested and Shapiro and Kanak (2002) showed that vertical vorticity could be generated through the tilting of solenoidally generated horizontal vorticity formed on the edges of buoyant thermals by the horizontal gradients of vertical velocity associated with these convective elements.

Though tilting of solenoidal horizontal vorticity may play a role in our simulations, analysis of the results suggests that the tilting of ambient horizontal vorticity associated with the mean wind shear by rolls is the dominant initial source of vertical vorticity. Profiles of the mean horizontal vorticity components (ξ, η) are shown in Fig. 8 at $t = 2.5$ h in the parallel-roll simulation. This time is just prior to the onset of robust boundary layer convection, such that horizontal gradients in vertical velocity and horizontal wind perturbations are small. The easterly vertical shear (with little southerly shear) in the parallel-roll boundary layer results in horizontal vorticity that is almost exclusively northerly ($\eta < 0$; Fig. 8). The large amount of northerly horizontal vorticity near the surface evident in Fig. 8 reflects the effects of surface drag below the lowest grid level ($z = 25$ m).

Under the inviscid Boussinesq approximation for a nonrotating reference frame, local changes in vorticity

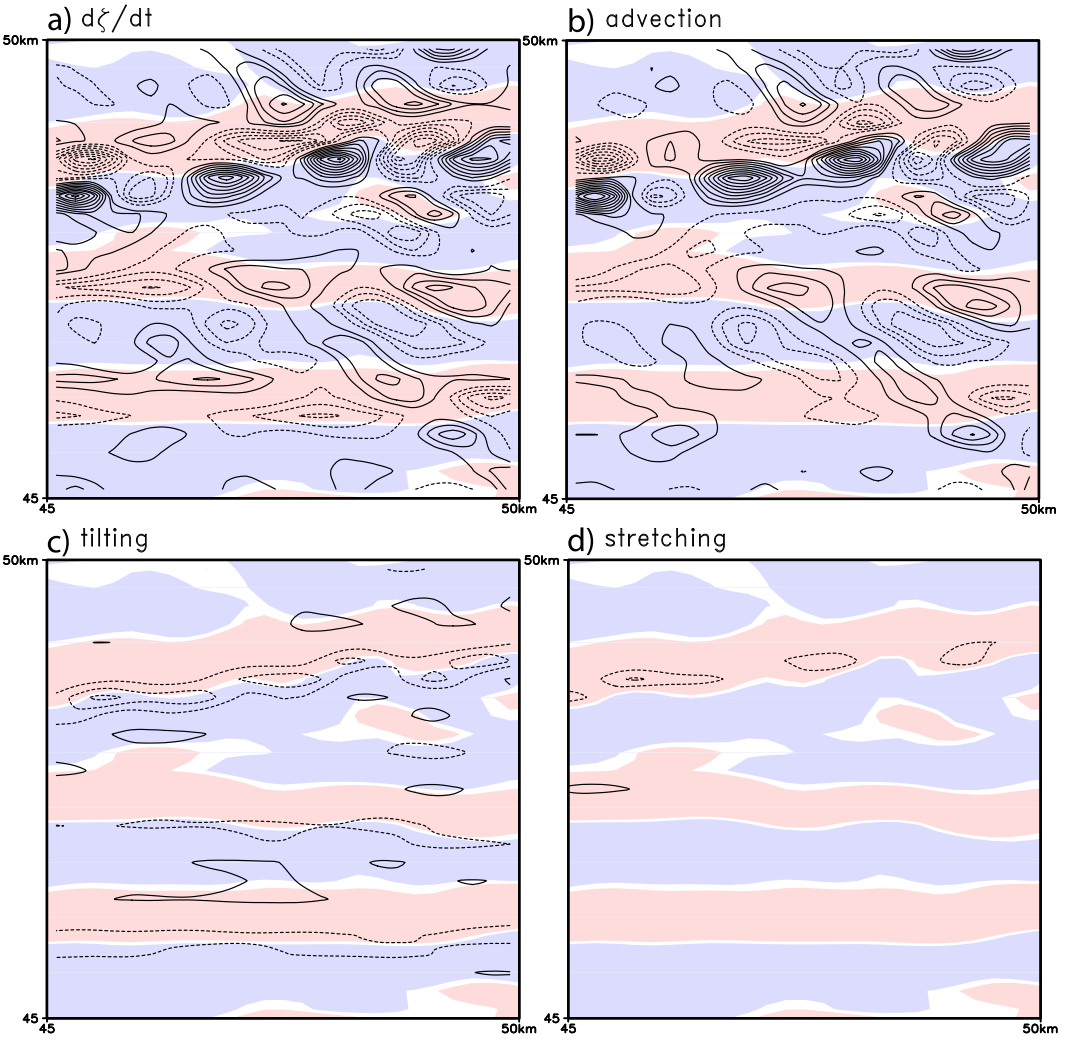

FIG. 12. As in Fig. 11, but at 3.25 h. Note that all contours are now at $3 \times 10^{-5}\,\mathrm{s}^{-2}$ intervals.

[$\boldsymbol{\omega}$ ($= \xi\mathbf{i} + \eta\mathbf{j} + \zeta\mathbf{k}$)] are described by the following equations (Markowski and Richardson 2010):

$$\frac{\partial \xi}{\partial t} = -\mathbf{v}\cdot\nabla\xi + \boldsymbol{\omega}\cdot\nabla u + \frac{\partial B}{\partial y}, \tag{5}$$

$$\frac{\partial \eta}{\partial t} = -\mathbf{v}\cdot\nabla\eta + \boldsymbol{\omega}\cdot\nabla v - \frac{\partial B}{\partial x}, \tag{6}$$

$$\frac{\partial \zeta}{\partial t} = -\mathbf{v}\cdot\nabla\zeta + \xi\frac{\partial w}{\partial x} + \eta\frac{\partial w}{\partial y} + \zeta\frac{\partial w}{\partial z}, \tag{7}$$

where B is the buoyancy ($=g\theta'_\rho/\theta_{\rho_0}$).[6]

[6] Here θ_ρ is the density potential temperature ($\theta_\rho = \theta[(1 + q_v/\varepsilon)/(1 + q_t)]$, where q_t is the total water mixing ratio and ε is the ratio of the gas constants for dry air and water vapor).

The evolution of the horizontal and vertical vorticity fields as boundary layer convection intensifies is shown in Fig. 9. At 2.25 h (Fig. 9a) horizontal vorticity at z = 125 m is northerly and relatively uniform throughout the domain, and there is some evidence of vertical vorticity development at this height near bands of weak vertical velocity (evident by patches of $|w| > 0.1\,\mathrm{m\,s}^{-1}$).

Vertical velocity begins to increase in intensity and coverage at 2.5 h (Fig. 9b). While predominately northerly, the vorticity begins to acquire a zonal component ξ. This is due to horizontal tilting of meridional vorticity η by gradients in velocity along the roll updraft/downdraft interfaces [the second term on the right in (5)] as well as solenoidal generation from meridional buoyancy gradients [the third term on the right in (5); recall periodic potential temperature gradients associated with the roll circulations].

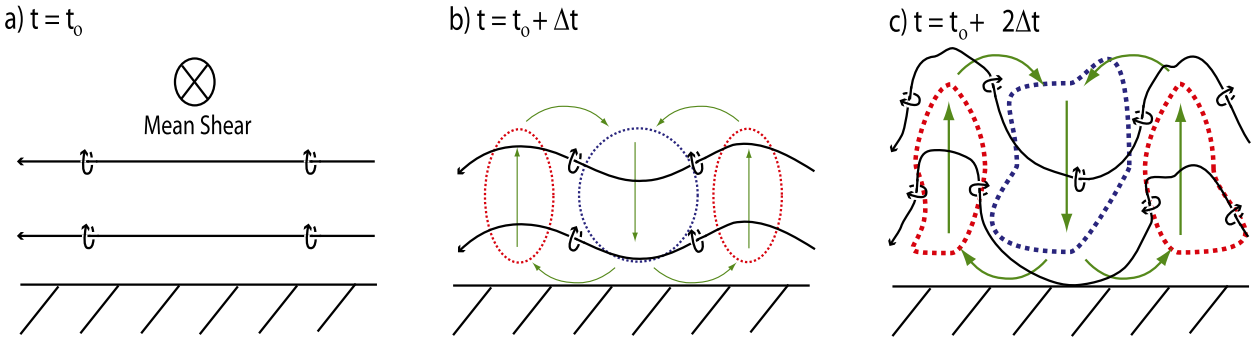

FIG. 13. Conceptual illustration of vertical vorticity generation in a CBL with rolls. (a) Mean shear into the page is associated with horizontal vortex lines (black lines) and no preexisting vertical vorticity. (b) At a later time, weak dry boundary layer convection develops and organizes into rolls parallel to the shear vector. Perturbation vertical velocity associated with the rolls (green arrows) tilts the horizontal vortex lines associated with the mean flow. Periodic bands of positive and negative vertical vorticity result between updraft (red) and downdraft (blue) regions. (c) Roll circulations intensify, deepening the boundary layer, and become more disorganized. While tilting still occurs, vertical vorticity is chaotically reoriented, redistributed, and amplified by advection and stretching. By this time, vortex lines have a significant component normal to the plane shown owing to baroclinic generation of horizontal vorticity (of similar sense to the circulations shown with green arrows) between the roll updraft and downdraft regions.

Alternating bands of positive and negative vertical vorticity ζ are also clearly evident at this time. Vertical cross sections along the meridional axis (Fig. 10a) show that these bands extend through the depth of the CBL. Furthermore, the mechanism for the development of ζ becomes qualitatively apparent when one considers the tilting of vorticity vectors in the plane of the cross section by updrafts and downdrafts, a manifestation of the third term on the right side of (7). Tilting of horizontal vorticity [the combination of the second and third terms on the right side of (7)] is explicitly calculated and shown in Fig. 10b, indicating that tilting creates positive (negative) vertical vorticity on the right (left) side of updrafts, looking downshear. When compared with stretching [fourth term on the right side of (7); Fig. 11d] at 2.5 h, tilting (Fig. 11c) and advection [first term on the right side of (7); Fig. 11b] are the primary contributors to the local vertical vorticity tendency (Fig. 11a). This suggests that the initial vertical vorticity in the CBL originates from the tilting of environmental horizontal vorticity by the developing thermals and compensating downdrafts. Near the surface ($z \lesssim 100$ m), downdrafts are necessary for the development of vertical vorticity, because tilting of horizontal vorticity by an updraft alone cannot produce appreciable vertical vorticity near the ground owing to the advection of vertical vorticity away from the ground in an updraft (e.g., Davies-Jones 1982; Davies-Jones et al. 2001).

Robust boundary layer convection ($w_{\max} > 1\,\mathrm{m\,s^{-1}}$ within the CBL) has developed by 3.25 h (Fig. 9c). Between 2.5 and 3.25 h, the pattern of local changes in vertical vorticity has become more three-dimensional (Fig. 12a, note the increased magnitude of the contours in Fig. 12 relative to Fig. 11), largely due to the dominant advection term (Fig. 12b). Thus, though still largely arranged in periodic bands, local maxima and minima of vertical vorticity have begun to arise by 3.25 h (Fig. 9c). Baroclinically generated perturbations to the horizontal vorticity associated with the rolls themselves are visible in the now-distinct zonal component of the horizontal vorticity vectors, particularly between updrafts and downdrafts. Without a mechanism for maintaining the initial background vertical wind shear in the model (there are no large-scale horizontal pressure gradients in the base state), there is now less meridional vorticity η to be tilted into the vertical by the largely meridional vertical velocity gradients. Consequently, tilting (Fig. 12c) has become a smaller portion of the vertical vorticity tendency (Fig. 12a) than advection (Fig. 12b). Stretching (Fig. 12d), though now of similar magnitude as tilting, remains a small contributor to the local vertical vorticity tendency. By 4.0 h, the rolls continue to become less organized while local maxima/minima of vorticity become stronger and more three-dimensional (Fig. 9d).

The process of vertical vorticity generation in a CBL with mean shear and rolls is summarized conceptually in Fig. 13. Initially, the mean boundary layer shear is associated with purely horizontal vorticity (Fig. 13a). As weak thermals develop, this vorticity is tilted by the thermals and compensating downdraft regions, resulting in periodic bands of weak positive and negative vertical vorticity (Fig. 13b). This is the same process Marquis et al. (2007) suggested to explain their observations of vertical vorticity in convective boundary layers. The rolls intensify, developing along-roll perturbation horizontal vorticity and becoming more disorganized as the boundary layer deepens (Fig. 13c). Tilting of cross-roll vorticity may still occur, but considerable along-roll

perturbations lead to a somewhat chaotic redistribution of vertical vorticity into vorticity extrema through advection, tilting, and stretching similar to the vorticity dynamics observed by Markowski and Hannon (2006) or postulated by Maxworthy (1973).

5. Sensitivity to grid spacing

In this section we explain how we determined that 200-m horizontal grid spacing (Δ_h) is adequate for our studies of supercells in an environment with a CBL. Toward this end, we present results from three CBL simulations that were conducted using $\Delta_h = 100$, 200, and 500 m (Fig. 14). These simulations are evaluated with regards to the underlying assumptions of LES and the ability of the simulated flows to produce the scales of motion expected by theory and observations of boundary layer rolls.

Because of the current impracticality of direct numerical simulation (DNS), we use LES, for which the Navier–Stokes equations are filtered and the subfilter-scale effects are parameterized. [Reviews of LES principles are available in several textbooks, e.g., Wyngaard (2010).] Following Bryan et al. (2003), we determine an appropriate value of Δ_h by examining properties of the flow from these sensitivity simulations. For their simulations of deep moist convection, Bryan et al. (2003) concluded that Δ_h of $O(100)$ m produced results that meet the assumptions inherent in LES. One of these assumptions is that $l/\Delta \gg 1$, where l represents the scale of large energy-containing eddies, and $\Delta = (\Delta x \Delta y \Delta z)^{1/3}$ is a characteristic grid scale and roughly equal to the implicit LES filter width. The criterion $l/\Delta \gg 1$ ensures that the simulated flow has a large effective Reynolds number [see Eq. (12) in Bryan et al. (2003)], and thus the resolved component of the simulated flow can be turbulent.

Table 2 shows Δ for each CBL sensitivity simulation, and an estimate of the ratio l/Δ for both deep convection and for the CBL. For deep convection we assume $l \approx 10$ km (following Bryan et al. 2003), and for the CBL we assume $l \approx 1$ km. For deep convection, the values of l/Δ (Table 2) are larger than 10, and so LES of deep convection should be adequate in all three cases. For the CBL, $\Delta_h = 500$ m seems clearly inappropriate because $l/\Delta = 4$.[7] Vertical velocity from our simulation with $\Delta_h = 500$ m (Fig. 14c) shows that roll-like structures form, although they are qualitatively smooth, and seem more characterizable as laminar rather than turbulent. For

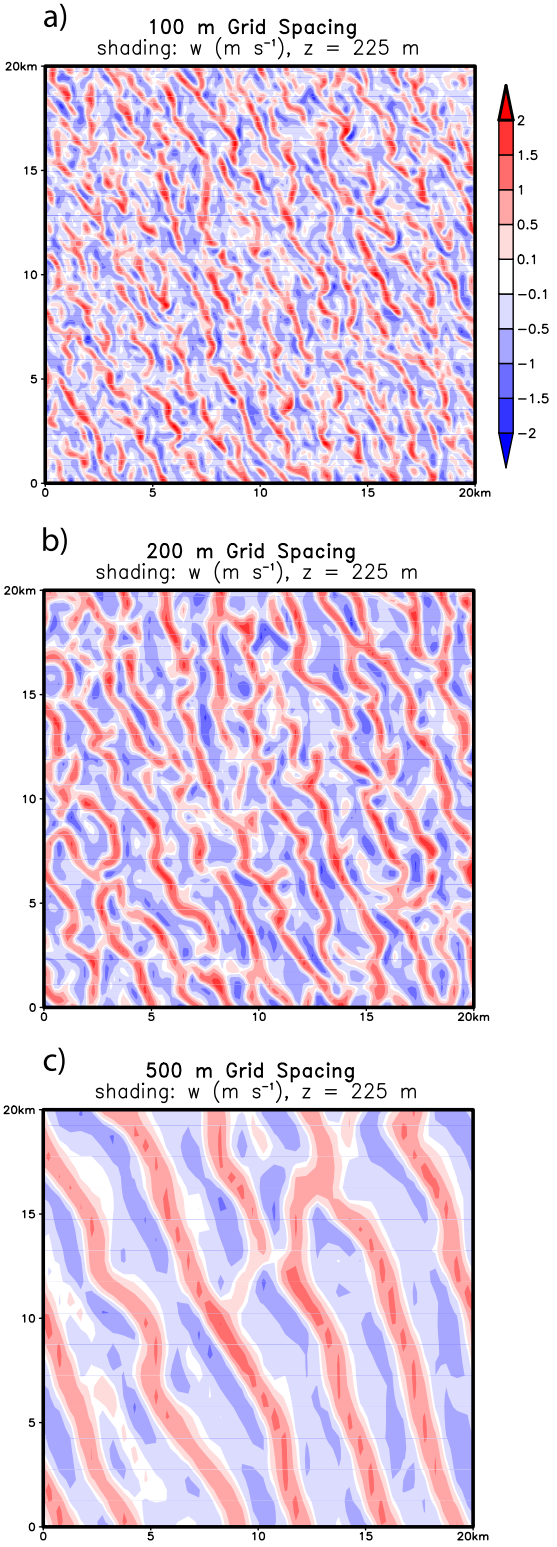

FIG. 14. Plan view of vertical velocity (m s^{-1}, shaded) 225 m above the lower model surface 1 h after the development of boundary layer convection for the CBL test simulations with (a) 100-m horizontal grid spacing at $t = 3.0$ h, (b) 200-m horizontal grid spacing at $t = 3.75$ h, and (c) 500-m horizontal grid spacing at $t = 5.75$ h.

[7] Here Δ also depends on the vertical grid spacing Δz. In all of our simulations $\Delta z = 50$ m, such that changes in Δ are due only to modifications of Δ_h.

TABLE 2. Relevant parameters for assessing LES applicability of simulations with different horizontal grid spacing.

Horizontal grid spacing	Δ	Deep convection l/Δ	CBL l/Δ	Min SGS	Avg SGS
100 m	79 m	127	13	13%	20%
200 m	126 m	80	8	16%	29%
500 m	232 m	43	4	24%	40%

Δ_h = 100 and 200 m, values of l/Δ are $O(10)$ (Table 2). Ideally, this ratio should be $O(100)$ (or greater). Nevertheless, the simulated flows for Δ_h = 100 and 200 m (Figs. 14a,b) seem qualitatively different from the flow in the coarsest-resolution simulation (Fig. 14c), particularly in the sense that turbulent eddies with horizontal scale of $O(1)$ km exist, in addition to the linear roll structures. In other words, the flow is qualitatively turbulent.

Considering also that l/Δ is $O(10)$ for Δ_h = 100 and 200 m, and the *effective Reynolds number of LES* R_t varies as $(l/\Delta)^{4/3}$ [Eq. (12) of Bryan et al. (2003)], these simulations are probably best characterized as low-R_t LES. We assume that mean properties of the flow would remain the same for smaller grid spacing [i.e., larger R_t (e.g., Bryan et al. 2003)]. In a recent numerical study of CBLs (without vertical wind shear), Sullivan and Patton (2011) found that simulations with relatively low R_t (or, in their terminology, relatively low "large-eddy Reynolds number") produce qualitatively accurate profiles of heat flux and total turbulent kinetic energy, although the boundary layer depth increased too quickly, and higher-order metrics like skewness were overestimated. Unfortunately, smaller Δ_h is not currently feasible for the size, duration, and number of simulations required by our experimental design. The effect of these biases on our results will thus need to be reassessed with smaller Δ_h (i.e., larger R_t) in a future study.

Another means of assessing LES is by comparing the ratio of parameterized SGS TKE (e_s) to resolved-scale TKE (e_r). Total TKE (E) is given by $E = e_r + e_s$. In this study, $e_r(x, y, z, t) = 1/2(\overline{u'u'} + \overline{v'v'} + \overline{w'w'})$, where u',v', w' are the deviations of the model-produced velocities at each grid point from their respective horizontal averages at each height level, and $e_s(x, y, z, t)$ is determined by the subgrid turbulence model [similar to Deardorff (1980); the user is referred to Bryan (2009) for the precise formulation].

Figure 15 shows time–height series of horizontally averaged E over the course of the CBL sensitivity simulations. For the first few hours, E is limited to the lowest few hundred meters in all simulations and is predominantly subgrid scale (i.e., $e_s \gg e_r$, not shown). There is a rapid increase and deepening in E when the rolls develop, and e_r becomes comparable to (or exceeds) e_s;

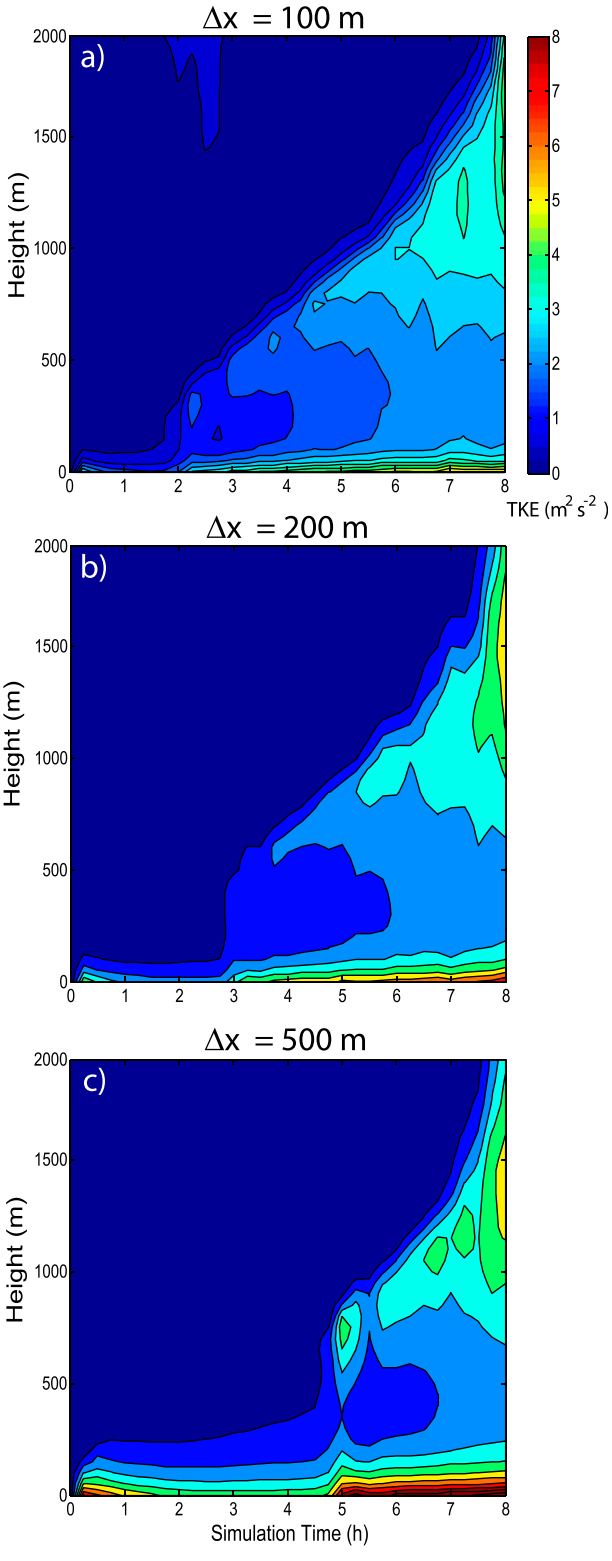

FIG. 15. Time–height series of the horizontally averaged total TKE [$\overline{E}(z, t)$; m^2 s^{-2}] at each vertical grid level over the simulation duration for CBL test simulations with (a) 100-, (b) 200-, and (c) 500-m horizontal grid spacing.

the time when this transition occurs is later as Δ_h increases (cf. Figs. 15a,c).

By integrating all measures of TKE over the domain from 0 to 2 km AGL, and plotting the results over time (Fig. 16), it becomes apparent that e_s is the dominant contributor to E early (i.e., $t \lesssim 3$ h) and remains nearly constant throughout the simulations. In contrast, e_r is the dominant contributor to E for $t \gtrsim 3$ h, and continually increases with time. A desirable ratio of e_s to E is about 10% or less (e.g., Bryan et al. 2003). Table 2 lists minimum and average values (for $t \gtrsim 4$ h) of the ratio e_s/E for each simulation. Consistent with our analysis of l/Δ above, none of these simulations has $e_s/E < 0.1$, although the highest-resolution simulation is close, and the lowest-resolution simulation is clearly not adequate for LES.

As previously stated, it is not practical (at this time) to run simulations with smaller Δ_h to better satisfy the underlying assumptions of LES for boundary layer convection; Δ_h of $O(10)$ m would be ideal. However, our analysis reaffirms that Δ_h of $O(100)$ m meets requirements for LES of deep convection. Also, our nominal grid spacing ($\Delta_h = 200$ m) is similar, or smaller, than Δ_h used in previous simulation studies of rolls over large domains (>100 km^2) (e.g., Weckwerth et al. 1997; Fovell and Dailey 2001; Peckham et al. 2004; Xue and Martin 2006a). Indeed, some of these studies have noted disparity between their results and nature. Peckham et al. (2004; $\Delta_h = 1$ km) noted rolls with aspect ratios larger than those observed and predicted by theory and suggested this discrepancy was "possibly due in part to the model's inability to fully resolve boundary-layer circulations at the scale of the horizontal grid resolution." Ziegler et al. (1997; $\Delta_h = 1$ km) attributed larger-than-expected wavelengths to both insufficient resolution and potential interaction with gravity waves in the capping inversion. Nevertheless, Weckwerth et al. (1997) were able to simulate rolls of realistic dimensions using $\Delta_h = 250$ m. Periodic boundary conditions may also affect roll aspect ratio and orientation because of quantization effects due to the requirement that the number of rolls be an integer and rolls reenter the domain at the same location they left on the opposite side (Young et al. 2002).

To further evaluate whether the simulated rolls adequately represent those in nature, we check for consistency with observations and theory. Figure 17 shows times series of (Fig. 17a) the boundary layer depth z_i, (Fig. 17b) the roll wavelength λ, and (Fig. 17c) the roll aspect ratio λ/z_i. The wavelength of rolls is determined subjectively by counting the number of roll updraft branches along a 20-km line perpendicular to the axis of the rolls, and then dividing 20 km by the number of updraft branches. This technique is repeated for three different cross-section locations, with the final reported value being the average of the three measurements.

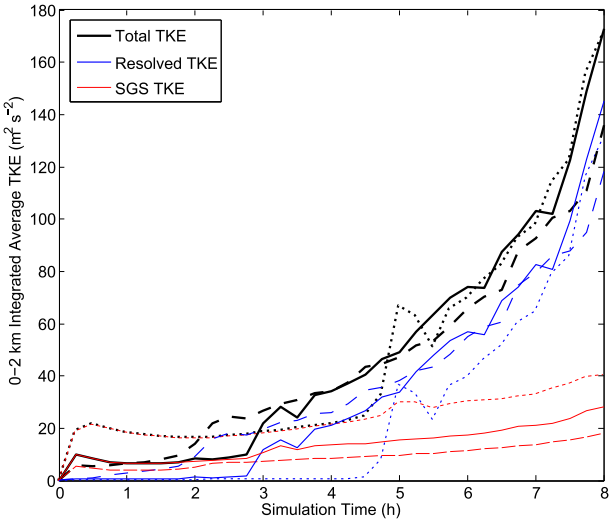

FIG. 16. Time series of horizontally averaged total (thick black), resolved (medium blue), and SGS (thin red) TKE integrated over the lowest 2 km of the model domain for CBL test simulations with 100- (long dashed), 200- (solid), and 500-m (short dashed) horizontal grid spacing.

Boundary layer depth z_i increases at a similar rate for all three sensitivity simulations (Fig. 17a), especially for $t > 3$ h. As noted previously, rolls develops at later times as Δ_h increases, which can be seen by the initial time that λ is plotted in Fig. 17b. We further note that the minimum wavelength resolvable in this numerical model is $\sim 7\Delta_h$ [e.g., appendix in Bryan et al. (2003)]. Thus, rolls should not be expected to develop in any simulation until the theoretical wavelength (green in Fig. 17b, explained below) is at least $7\Delta_h$; this conclusion is supported by the correspondence of the green line with the highest-resolution model results in Fig. 17b.

Assuming the longitudinal rolls in this simulation are forced primarily by convective instability, linear theory suggests an aspect ratio $\lambda/z_i = 2.83$ (e.g., Rayleigh 1916; Asai 1970). Assuming this aspect ratio, the predicted roll wavelength $\lambda = 2.83 z_i$ is assumed for the theoretical wavelength, and is shown in green in Fig. 17b. Rolls in the 500-m simulation clearly have an unrealistically large wavelength, again supporting the conclusion that $\Delta_h = 500$ m is inadequate for our work. As Δ_h decreases, both the wavelength (Fig. 17b) and aspect ratio (Fig. 17c) of the rolls appear to converge toward the theoretical values (green line). By these measures, it appears that either $\Delta_h = 100$ or 200 m should be adequate for simulations of boundary layer rolls.

The rolls in these simulations last for ~2 h before losing recognizable two-dimensionality. This transition

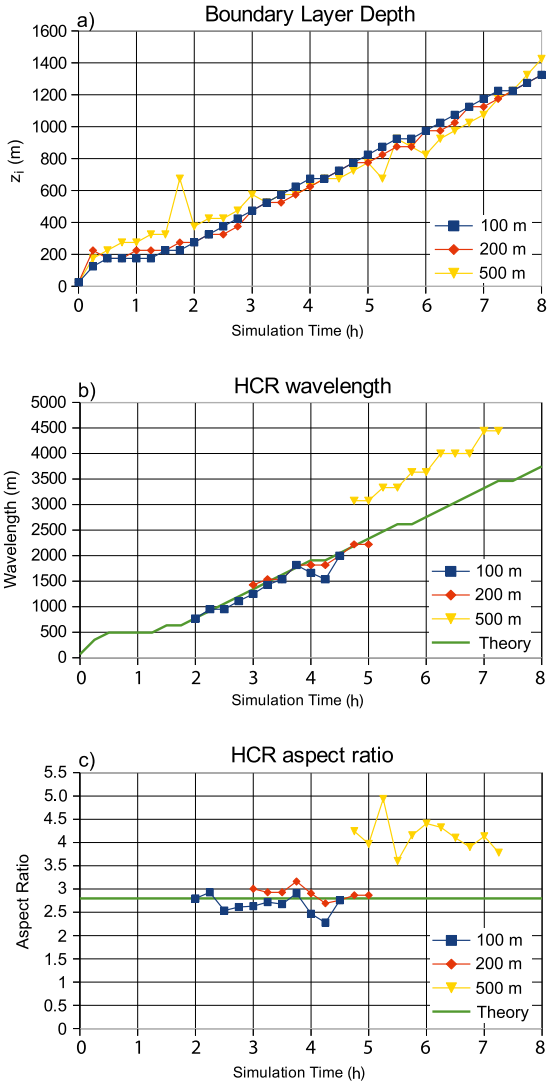

FIG. 17. Time series of (a) boundary layer depth, (b) roll wavelength, and (c) roll aspect ratio (wavelength/z_i) for the CBL test simulations. In (b) and (c), time series of the wavelength and aspect ratio predicted by theory based on the average boundary layer growth of the three simulations are shown in green.

is probably associated with increasing boundary layer instability relative to the effects of shear (e.g., Ferrare et al. 1991; Weckwerth et al. 1999), which can be described by the ratio of z_i to the Obukhov length L defined as

$$L = -\frac{\overline{\theta} u_*^3}{kg\overline{w'\theta'}|_s}, \tag{8}$$

where $k = 0.4$ is the von Kármán constant, $u_* = (\overline{u'w'}|_s^2 + \overline{v'w'}|_s^2)^{1/4}$ is the friction velocity, and $\overline{w'\theta'}|_s$ is the surface heat flux (Stull 1988). Quantities with overbars

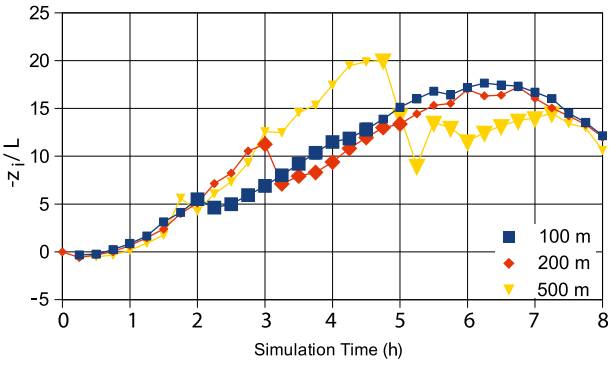

FIG. 18. Time series of the negative ratio of boundary layer depth to Obukhov length for each CBL test simulation. Large markers indicate periods when rolls are clearly present.

are horizontal averages. Under convective conditions, the magnitude of the Obukhov length decreases as the buoyant production of TKE exceeds its shear production in the surface layer, such that $-z_i/L$ increases as buoyancy forcing dominates shear forcing throughout the CBL.

There is a wide range of observed values for z_i/L that are conducive to rolls. Observations summarized by Etling and Brown (1993) concluded that rolls driven largely by convective instability exist when $5 < -z_i/L < 25$. They noted it was possible that rolls driven by dynamic instabilities may exist at smaller values of $-z_i/L$. In this study, rolls generally exist with $-z_i/L$ in the range suggested by Etling and Brown (Fig. 18). Roll formation occurs when $-z_i/L > 5$ (excluding the $\Delta_h = 500$-m simulation) and rolls are no longer apparent when $-z_i/L > 15$ (for all grid spacings). Sharp decreases in $-z_i/L$ occur at the onset of resolved turbulence in each simulation. These sharp decreases appear to be caused by abrupt changes in the friction velocity and surface-layer heat flux associated with the sharp increase in e_r at this time. The sharp decreases are more abrupt with coarser resolution. The duration of rolls in these simulations is somewhat shorter than in nature, possibly due to the lack of a large-scale (synoptic) horizontal pressure gradient in the model that could counteract the vertical mixing of momentum and thus sustain the low-level shear for a longer time.

6. Conclusions

In this study, a convective boundary layer (CBL) composed of quasi-two-dimensional, horizontal roll vortices was simulated over a large domain, including radiation and surface fluxes of heat, moisture, and momentum with idealized mean thermodynamic and wind profiles supportive of supercell thunderstorms. This article focuses

on properties of the simulated boundary layer in the absence of a supercell (which will be studied in a forthcoming article).

The simulated rolls result in quasi-periodic horizontal variations in boundary layer potential temperature (± 0.5 K), boundary layer water vapor mixing ratio ($\pm 0.5\,g\,kg^{-1}$), CAPE ($\pm 150\,J\,kg^{-1}$), CIN ($\pm 10\,J\,kg^{-1}$), vertical velocity ($\pm 5\,m\,s^{-1}$), and 0–1-km SRH ($\pm 50\,m^2\,s^{-2}$). These variations are consistent with previous observations of rolls and suggest that a supercell may encounter nonnegligible variability in parameters that have previously been demonstrated to influence supercell evolution. Markowski and Richardson (2007) found that "in some of the cases in which mesoscale boundaries were present, the variability that can be attributed to boundary layer convection is as significant as that which can be attributed to the differing air masses." Considering that previous studies have determined that mesoscale boundaries could influence supercell properties, particularly low-level rotation, perhaps the similar environmental heterogeneity found in the CBL documented here could also affect supercells.

The simulated rolls are also a source of environmental vertical vorticity in the boundary layer. It was found that bands of alternating positive/negative vertical vorticity originate through the tilting of cross-roll horizontal vorticity in the boundary layer associated with the environmental vertical wind shear, which is enhanced in these simulations by surface drag. Once formed, vertical vorticity may be rearranged and amplified into local vorticity extrema ($\zeta > 0.01\,s^{-1}$) through advection and stretching. The presence of vertical vorticity in the CBL is important because most conceptual models and numerical simulations of supercell tornadogenesis assume an ambient environment devoid of vertical vorticity. Whereas boundary layer heterogeneity and vorticity extrema have been linked to the evolution of misocyclones along mesoscale boundaries (e.g., Wilson et al. 1992; Atkins et al. 1995; Arnott et al. 2006; Marquis et al. 2007), to this point, it has been unclear what effects (if any) CBL vorticity extrema may have on supercells and their mesocyclones.

Sensitivity studies suggest that horizontal grid spacing $\leq$200 m is required for adequate resolution of rolls under the considered conditions. Present-day computing resources allow for multiple large-domain supercell simulations with 200-m horizontal grid spacing, and based on this result we use this spacing for our subsequent work. Deep moist convection can now be initiated using the simulated CBL as the base state to investigate the interactions between an organized CBL and mature supercell thunderstorms. Results of these experiments are detailed in Nowotarski (2013) and will be the subject of future publications.

Acknowledgments. The authors thank Drs. Nels Shirer, Lyle Long, Morris Weisman, Tammy Weckwerth, Marcelo Chamecki, and David Stensrud for many helpful suggestions throughout the course of this project. We also appreciate thoughtful suggestions for improvements to this manuscript from the three anonymous reviewers. This work was supported by NSF Grant AGS-0644533. Richardson's time was supported by NSF Grant AGS-1157646. Computational resources and travel support also were provided by the National Center for Atmospheric Research. Many of the figures in this manuscript were created using the Grid Analysis and Display System (GrADS) developed by the Center for Ocean–Atmosphere–Land Studies.

REFERENCES

Arakawa, A., and V. Lamb, 1977: Computational design of the basic dynamical processes in the UCLA general circulation model. *General Circulation Models of the Atmosphere,* J. Chang, Ed., Vol. 17, *Methods in Computational Physics,* Academic Press, 174–264.

Arnott, N. R., Y. P. Richardson, J. M. Wurman, and E. M. Rasmussen, 2006: Relationship between a weakening cold front, misocyclones, and cloud development on 10 June 2002 during IHOP. *Mon. Wea. Rev.,* **134,** 311–335, doi:10.1175/MWR3065.1.

Asai, T., 1970: Stability of a plane parallel flow with variable vertical shear and unstable stratification. *J. Meteor. Soc. Japan,* **48,** 129–139.

Atkins, N. T., R. M. Wakimoto, and T. M. Weckwerth, 1995: Observations of the sea-breeze front during CaPE. Part II: Dual-Doppler and aircraft analysis. *Mon. Wea. Rev.,* **123,** 944–969, doi:10.1175/1520-0493(1995)123<0944:OOTSBF>2.0.CO;2.

——, M. L. Weisman, and L. J. Wicker, 1999: The influence of preexisting boundaries on supercell evolution. *Mon. Wea. Rev.,* **127,** 2910–2927, doi:10.1175/1520-0493(1999)127<2910:TIOPBO>2.0.CO;2.

Atkinson, B. W., and J. W. Zhang, 1996: Mesoscale shallow convection in the atmosphere. *Rev. Geophys.,* **34,** 403–431, doi:10.1029/96RG02623.

Atlas, D., S. H. Chou, and P. J. Sheu, 1986: The structure of the unstable marine boundary layer viewed by lidar and aircraft observations. *J. Atmos. Sci.,* **43,** 1301–1318, doi:10.1175/1520-0469(1986)043<1301:TSOTUM>2.0.CO;2.

Brown, R. A., 1972: On the inflection point instability of a stratified Ekman boundary layer. *J. Atmos. Sci.,* **29,** 850–859, doi:10.1175/1520-0469(1972)029<0850:OTIPIO>2.0.CO;2.

——, 1980: Longitudinal instabilities and secondary flows in the planetary boundary layer: A review. *Rev. Geophys. Space Phys.,* **18,** 683–697, doi:10.1029/RG018i003p00683.

Bryan, G. H., 2002: An investigation of the convective region of numerically simulated squall lines. Ph.D. thesis, The Pennsylvania State University, 181 pp.

——, 2009: The governing equations for CM1. National Center for Atmospheric Research, Boulder, CO, 15 pp.

——, and J. M. Fritsch, 2002: A benchmark simulation for moist nonhydrostatic numerical models. *Mon. Wea. Rev.,* **130,** 2917–2928, doi:10.1175/1520-0493(2002)130<2917:ABSFMN>2.0.CO;2.

——, J. C. Wyngaard, and J. M. Fritsch, 2003: Resolution requirements for the simulation of deep moist convection. *Mon. Wea.*

Rev., **131,** 2394–2416, doi:10.1175/1520-0493(2003)131<2394:RRFTSO>2.0.CO;2.

Buban, M. S., C. L. Ziegler, E. R. Mansell, and Y. P. Richardson, 2012: Simulation of dryline misovortex dynamics and cumulus formation. *Mon. Wea. Rev.,* **140,** 3525–3551, doi:10.1175/MWR-D-11-00189.1.

Carpenter, R. L., Jr., K. K. Droegemeier, and A. M. Blyth, 1998: Entrainment and detrainment in numerically simulated cumulus clouds. *J. Atmos. Sci.,* **55,** 3417–3432, doi:10.1175/1520-0469(1998)055<3417:EADINS>2.0.CO;2.

Chou, M. D., and M. J. Suarez, 1999: A solar radiation parameterization for atmospheric studies. NASA Tech. Rep. 15, 38 pp.

——, ——, C. H. Ho, M. M. Yan, and K. T. Lee, 1998: Parameterizations for cloud overlapping and shortwave single-scattering properties for use in general circulation and cloud ensemble models. *J. Climate,* **11,** 202–214, doi:10.1175/1520-0442(1998)011<0202:PFCOAS>2.0.CO;2.

——, K. T. Lee, S. C. Tsay, and Q. Fu, 1999: Parameterization for cloud longwave scattering for use in atmospheric models. *J. Climate,* **12,** 159–169, doi:10.1175/1520-0442-12.1.159.

Conzemius, R. J., and E. Fedorovich, 2008: A case study of convective boundary layer development during IHOP_2002: Numerical simulations compared to observations. *Mon. Wea. Rev.,* **136,** 2305–2320, doi:10.1175/2007MWR2193.1.

Craven, J. P., and H. E. Brooks, 2004: Baseline climatology of sounding derived parameters associated with deep, moist convection. *Natl. Wea. Dig.,* **28,** 13–24.

Crook, N. A., and M. L. Weisman, 1998: Comparison of supercell behavior in a convective boundary layer with that in a horizontally-homogeneous environment. Preprints, *19th Conf. on Severe Local Storms,* Minneapolis, MN, Amer. Meteor. Soc., 8.3.

Dailey, P. S., and R. G. Fovell, 1999: Numerical simulation of the interaction between the sea-breeze front and horizontal convective rolls. Part I: Offshore ambient flow. *Mon. Wea. Rev.,* **127,** 858–878, doi:10.1175/1520-0493(1999)127<0858:NSOTIB>2.0.CO;2.

Davies-Jones, R., 1982: Observational and theoretical aspects of tornadogenesis. *Intense Atmospheric Vortices,* L. Bengtsson and J. Lighthill, Eds., Springer-Verlag, 175–189.

——, R. J. Trapp, and H. B. Bluestein, 2001: Tornadoes and tornadic storms. *Severe Convective Storms, Meteor. Monogr.,* No. 50, Amer. Meteor. Soc., 167–221.

Deardorff, J. W., 1974: Three-dimensional numerical study of the height and mean structure of a heated planetary boundary layer. *Bound.-Layer Meteor.,* **7,** 81–106, doi:10.1007/BF00224974.

——, 1980: Stratocumulus-capped mixed layers derived from a three-dimensional model. *Bound.-Layer Meteor.,* **18,** 495–527, doi:10.1007/BF00119502.

Etling, D., and R. A. Brown, 1993: Roll vortices in the planetary boundary layer: A review. *Bound.-Layer Meteor.,* **65,** 215–248, doi:10.1007/BF00705527.

Faller, A. J., 1965: Large eddies in the atmospheric boundary layer and their possible role in the formation of cloud rows. *J. Atmos. Sci.,* **22,** 176–184, doi:10.1175/1520-0469(1965)022<0176:LEITAB>2.0.CO;2.

Ferrare, R. A., J. L. Schols, E. W. Eloranta, and R. Coulter, 1991: Lidar observations of banded convection during BLX83. *J. Appl. Meteor.,* **30,** 312–326, doi:10.1175/1520-0450(1991)030<0312:LOOBCD>2.0.CO;2.

Foster, R. C., 2005: Why rolls are prevalent in the hurricane boundary layer. *J. Atmos. Sci.,* **62,** 2647–2661, doi:10.1175/JAS3475.1.

Fovell, R. G., and P. S. Dailey, 2001: Numerical simulation of the interaction between the sea-breeze front and horizontal convective rolls. Part II: Alongshore ambient flow. *Mon. Wea. Rev.,* **129,** 2057–2072, doi:10.1175/1520-0493(2001)129<2057:NSOTIB>2.0.CO;2.

Grell, G. A., J. Dudhia, and D. R. Stauffer, 1994: A description of the fifth-generation Penn State/NCAR Mesoscale Model (MM5). NCAR Tech. Note NCAR/TN-398+STR, 121 pp.

Haack, T., and H. N. Shirer, 1992: Mixed convective-dynamic roll vortices and their effects on initial wind and temperature profiles. *J. Atmos. Sci.,* **49,** 1181–1201, doi:10.1175/1520-0469(1992)049<1181:MCRVAT>2.0.CO;2.

Kanak, K. M., D. K. Lilly, and J. T. Snow, 2000: The formation of vertical vortices in the convective boundary layer. *Quart. J. Roy. Meteor. Soc.,* **126,** 2789–2810, doi:10.1002/qj.49712656910.

Klemp, J. B., and R. B. Wilhelmson, 1978: The simulation of three-dimensional convective storm dynamics. *J. Atmos. Sci.,* **35,** 1070–1096, doi:10.1175/1520-0469(1978)035<1070:TSOTDC>2.0.CO;2.

Kuettner, J. P., 1959: The band structure of the atmosphere. *Tellus,* **11,** 267–294, doi:10.1111/j.2153-3490.1959.tb00033.x.

——, 1971: Cloud bands in the earth's atmosphere. *Tellus,* **23,** 404–425, doi:10.1111/j.2153-3490.1971.tb00585.x.

Kuo, H. L., 1963: Perturbations of plane Couette flow in stratified fluid and origin of cloud streets. *Phys. Fluids,* **6,** 195–211, doi:10.1063/1.1706719.

LeMone, M. A., 1973: The structure and dynamics of horizontal roll vortices in the PBL. *J. Atmos. Sci.,* **30,** 1077–1091, doi:10.1175/1520-0469(1973)030<1077:TSADOH>2.0.CO;2.

——, and W. T. Pennell, 1976: The relationship of trade wind cumulus distribution to subcloud layer fluxes and structure. *Mon. Wea. Rev.,* **104,** 524–539, doi:10.1175/1520-0493(1976)104<0524:TROTWC>2.0.CO;2.

Lilly, D. K., 1966: On the instability of Ekman boundary flow. *J. Atmos. Sci.,* **23,** 481–494, doi:10.1175/1520-0469(1966)023<0481:OTIOEB>2.0.CO;2.

Lin, Y. L., R. D. Farley, and H. D. Orville, 1983: Bulk parameterization of the snow field in a cloud model. *J. Climate Appl. Meteor.,* **22,** 1065–1092, doi:10.1175/1520-0450(1983)022<1065:BPOTSF>2.0.CO;2.

Markowski, P. M., and C. Hannon, 2006: Multiple-Doppler radar observations of the evolution of vorticity extrema in a convective boundary layer. *Mon. Wea. Rev.,* **134,** 355–374, doi:10.1175/MWR3060.1.

——, and Y. P. Richardson, 2007: Observations of vertical wind shear heterogeneity in convective boundary layers. *Mon. Wea. Rev.,* **135,** 843–861, doi:10.1175/MWR3334.1.

——, and ——, 2010: *Mesoscale Meteorology in Midlatitudes.* Wiley-Blackwell, 407 pp.

——, C. Hannon, J. Frame, E. Lancaster, A. Pietrycha, R. Edwards, and R. Thompson, 2003: Characteristics of vertical wind profiles near supercells obtained from the Rapid Update Cycle. *Wea. Forecasting,* **18,** 1262–1272, doi:10.1175/1520-0434(2003)018<1262:COVWPN>2.0.CO;2.

Marquis, J. N., Y. P. Richardson, and J. M. Wurman, 2007: Kinematic observations of misocyclones along boundaries during IHOP. *Mon. Wea. Rev.,* **135,** 1749–1768, doi:10.1175/MWR3367.1.

Maxworthy, T., 1973: A vorticity source for large-scale dust devils and other comments on naturally occurring columnar vortices. *J. Atmos. Sci.,* **30,** 1717–1722, doi:10.1175/1520-0469(1973)030<1717:AVSFLS>2.0.CO;2.

Moeng, C. H., and J. C. Wyngaard, 1988: Spectral analysis of large-eddy simulations of the convective boundary layer. *J. Atmos. Sci.,* **45,** 3573–3587, doi:10.1175/1520-0469(1988)045<3573:SAOLES>2.0.CO;2.

——, and P. P. Sullivan, 1994: A comparison of shear- and buoyancy-driven planetary boundary layer flows. *J. Atmos. Sci.,* **51,** 999–1022, doi:10.1175/1520-0469(1994)051<0999:ACOSAB>2.0.CO;2.

Nowotarski, C. J., 2013: Simulating supercell thunderstorms in a convective boundary layer: Effects on storm and boundary layer properties. Ph.D. dissertation, Department of Meteorology, The Pennsylvania State University, 203 pp.

Peckham, S. E., R. B. Wilhelmson, L. J. Wicker, and C. L. Ziegler, 2004: Numerical simulation of the interaction between the dryline and horizontal convective rolls. *Mon. Wea. Rev.,* **132,** 1792–1812, doi:10.1175/1520-0493(2004)132<1792:NSOTIB>2.0.CO;2.

Rasmussen, E. N., and D. O. Blanchard, 1998: A baseline climatology of sounding-derived supercell and tornado forecast parameters. *Wea. Forecasting,* **13,** 1148–1164, doi:10.1175/1520-0434(1998)013<1148:ABCOSD>2.0.CO;2.

——, S. Richardson, J. M. Straka, P. M. Markowski, and D. O. Blanchard, 2000: The association of significant tornadoes with a baroclinic boundary on 2 June 1995. *Mon. Wea. Rev.,* **128,** 174–191, doi:10.1175/1520-0493(2000)128<0174:TAOSTW>2.0.CO;2.

Rayleigh, L., 1916: On convection currents in a horizontal layer of fluid when the higher temperature is on the underside. *Philos. Mag.,* **32,** 529–546, doi:10.1080/14786441608635602.

Reinking, R. F., R. J. Doviak, and R. O. Gilmer, 1981: Clear-air roll vortices and turbulent motions as detected with an airborne gust probe and dual-Doppler radar. *J. Appl. Meteor.,* **20,** 678–685, doi:10.1175/1520-0450(1981)020<0678:CARVAT>2.0.CO;2.

Richardson, Y. P., 1999: The influence of horizontal variations in vertical shear and low-level moisture on numerically simulated convective storms. Ph.D. dissertation, School of Meteorology, University of Oklahoma, 236 pp.

——, K. K. Droegemeier, and R. P. Davies-Jones, 2007: The influence of horizontal environmental variability on numerically simulated convective storms. Part I: Variations in vertical shear. *Mon. Wea. Rev.,* **135,** 3429–3455, doi:10.1175/MWR3463.1.

Shapiro, A., and K. M. Kanak, 2002: Vortex formation in ellipsoidal thermal bubbles. *J. Atmos. Sci.,* **59,** 2253–2269, doi:10.1175/1520-0469(2002)059<2253:VFIETB>2.0.CO;2.

Shirer, H. N., 1980: Bifurcation and stability in a model of moist convection in a shearing environment. *J. Atmos. Sci.,* **37,** 1586–1602, doi:10.1175/1520-0469(1980)037<1586:BASIAM>2.0.CO;2.

——, 1986: On cloud street development in three dimensions: Parallel and Rayleigh instabilities. *Contrib. Atmos. Phys.,* **59,** 126–149.

Stensrud, D. J., and H. N. Shirer, 1988: Development of boundary layer rolls from dynamic instabilities. *J. Atmos. Sci.,* **45,** 1007–1019, doi:10.1175/1520-0469(1988)045<1007:DOBLRF>2.0.CO;2.

Stull, R. B., 1988: *An Introduction to Boundary Layer Meteorology.* Kluwer Academic Publishers, 665 pp.

Sullivan, P. P., and E. G. Patton, 2011: The effect of mesh resolution on convective boundary layer statistics and structures generated by large-eddy simulation. *J. Atmos. Sci.,* **68,** 2395–2415, doi:10.1175/JAS-D-10-05010.1.

Tao, W. K., and J. Simpson, 1993: The Goddard Cumulus Ensemble Model. Part I: Model description. *Terr. Atmos. Oceanic Sci.,* **4,** 19–51.

——, S. Lang, J. Simpson, C. H. Sui, B. Ferrier, and M. D. Chou, 1996: Mechanisms of cloud–radiation interaction in the tropics and midlatitudes. *J. Atmos. Sci.,* **53,** 2624–2651, doi:10.1175/1520-0469(1996)053<2624:MOCRII>2.0.CO;2.

Thompson, R. L., R. Edwards, J. A. Hart, K. L. Elmore, and P. Markowski, 2003: Close proximity soundings within supercell environments obtained from the rapid update cycle. *Wea. Forecasting,* **18,** 1243–1261, doi:10.1175/1520-0434(2003)018<1243:CPSWSE>2.0.CO;2.

Weckwerth, T. M., J. W. Wilson, and R. M. Wakimoto, 1996: Thermodynamic variability within the convective boundary layer due to horizontal convective rolls. *Mon. Wea. Rev.,* **124,** 769–784, doi:10.1175/1520-0493(1996)124<0769:TVWTCB>2.0.CO;2.

——, ——, ——, and N. A. Crook, 1997: Horizontal convective rolls: Determining the environmental conditions supporting their existence and characteristics. *Mon. Wea. Rev.,* **125,** 505–526, doi:10.1175/1520-0493(1997)125<0505:HCRDTE>2.0.CO;2.

——, T. W. Horst, and J. W. Wilson, 1999: An observational study of the evolution of horizontal convective rolls. *Mon. Wea. Rev.,* **127,** 2160–2179, doi:10.1175/1520-0493(1999)127<2160:AOSOTE>2.0.CO;2.

Weisman, M. L., and J. B. Klemp, 1982: The dependence of numerically simulated convective storms on vertical wind shear and buoyancy. *Mon. Wea. Rev.,* **110,** 504–520, doi:10.1175/1520-0493(1982)110<0504:TDONSC>2.0.CO;2.

——, and ——, 1986: Characteristics of isolated convective storms. *Mesoscale Meteorology and Forecasting,* P. Ray, Ed., Amer. Meteor. Soc., 331–358.

Wicker, L. J., and W. C. Skamarock, 2002: Time-splitting methods for elastic models using forward time schemes. *Mon. Wea. Rev.,* **130,** 2088–2097, doi:10.1175/1520-0493(2002)130<2088:TSMFEM>2.0.CO;2.

Wilhelmson, R. B., and L. J. Wicker, 2001: Numerical modeling of severe local storms. *Severe Convective Storms, Meteor. Monogr.,* No. 50, Amer. Meteor. Soc., 123–166.

Wilson, J. W., G. B. Foote, N. A. Crook, J. C. Fankhauser, C. G. Wade, J. D. Tuttle, C. K. Mueller, and S. K. Krueger, 1992: The role of boundary-layer convergence zones and horizontal rolls in the initiation of thunderstorms: A case study. *Mon. Wea. Rev.,* **120,** 1785–1815, doi:10.1175/1520-0493(1992)120<1785:TROBLC>2.0.CO;2.

Wyngaard, J. C., 2010: *Turbulence in the Atmosphere.* Cambridge University Press, 393 pp.

Xue, M., and W. J. Martin, 2006a: A high-resolution modeling study of the 24 May 2002 dryline case during IHOP. Part I: Numerical simulation and general evolution of the dryline and convection. *Mon. Wea. Rev.,* **134,** 149–171, doi:10.1175/MWR3071.1.

——, and ——, 2006b: A high-resolution modeling study of the 24 May 2002 dryline case during IHOP. Part II: Horizontal convective rolls and convective initiation. *Mon. Wea. Rev.,* **134,** 172–191, doi:10.1175/MWR3072.1.

Young, G. S., D. A. R. Kristovich, M. R. Hjelmfelt, and R. C. Foster, 2002: Rolls, streets, waves, and more: A review of quasi-two-dimensional structures in the atmospheric boundary layer. *Bull. Amer. Meteor. Soc.,* **83,** 997–1001, doi:10.1175/1520-0477(2002)083<0997:RSWAMA>2.3.CO;2.

Ziegler, C. L., T. J. Lee, and R. A. Pielke, 1997: Convective initiation at the dryline: A modeling study. *Mon. Wea. Rev.,* **125,** 1001–1026, doi:10.1175/1520-0493(1997)125<1001:CIATDA>2.0.CO;2.